UNIVERSITÀ
DEGLI STUDI
DI PADOVA

Sede Amministrativa: Università degli Studi di Padova

Centro di Ateneo di Studi ed Attività Spaziali “Giuseppe Colombo” (CISAS)

SCUOLA DI DOTTORATO DI RICERCA IN : SCIENZE TECNOLOGIE E MISURE SPAZIALI
INDIRIZZO: SCIENZE E TECNOLOGIE PER LE APPLICAZIONI SATELLITARI E AERONAUTICHE
CICLO: XXVIII

OPTICAL SUBSYSTEMS OF METIS (MULTI ELEMENT TELESCOPE FOR IMAGING AND SPECTROSCOPY) ON BOARD OF THE SOLAR ORBITER MISSION

Direttore della Scuola : Ch.mo Prof. Giampiero Naletto
Coordinatore d’indirizzo: Ch.mo Prof. Giampiero Naletto
Supervisore: Ch.mo Prof. Giampiero Naletto
Co-supervisore: Dott.ssa Maria Guglielmina Pelizzo

Dottorando : Marco Nardello

Abstract

The Lyman-α spectral line, at 121.6 nm, is a wavelength of great interest for solar environment exploration and astrophysics. It is an important hydrogen emission line and can give information on the dynamics of heated regions of space like the solar photosphere and corona. Among others, the instrument METIS (Multi Element Telescope for Imaging and Spectroscopy) will be on board the mission Solar Orbiter, an ESA mission in collaboration with NASA, that from the year 2018 will undertake a trip towards the Sun to explore the dynamics of the solar dynamo and its connection with corona and heliosphere. METIS will take images of the corona in the visible range and at Lyman-α, studying shape and evolution of the processes expanding from the Sun to the heliosphere.

In the CNR-IFN UOS Padova laboratories I employed deposition and characterization facilities to study the characteristics of materials and devices to be used as optical elements at Lyman-α wavelength. A morphological characterization was carried on with an atomic force microscope (AFM) and an optical characterization revealed the performances of materials and devices. Variations in performances were related to modifications in the experimental conditions and the acquired knowledge was used to optimize the performances of the final product.

Annealing is an approach never fully explored before to increment the optical quality of magnesium fluoride thin films, and consequently the reflectivity of VUV optical elements. I conducted a study of the phenomena involved in the process and applied the procedure to the realization of improved mirrors for this spectral region. This work will present all the experimental steps that led to the realization of the final devices and describe the characteristics of this novel annealing approach.

Riassunto

La linea spettrale Lyman-α, a 121.6 nm, è una lunghezza d'onda di grande interesse per l'esplorazione dell'ambiente solare e per l'astrofisica. È un'importante linea di emissione dell'idrogeno e può dare informazioni sulle dinamiche di regioni calde dello spazio come la fotosfera solare e la corona. Lo strumento METIS (Multi Element Telescope for Imaging and Spectroscopy) sarà a bordo della missione Solar Orbiter, una missione dell'ESA in collaborazione con la NASA che dal 2018 intraprenderà un viaggio verso il Sole per esplorare le dinamiche della dinamo solare e la sua connessione con la corona e l'eliosfera. METIS acquisirà immagini nel visibile e alla lunghezza d'onda Lyman-α, studiando la forma e l'evoluzione dei processi in espansione dal Sole verso l'eliosfera.

Nei laboratori del CNR-IFN UOS Padova ho utilizato facility di deposizione e caratterizzazione per studiare le caratteristiche di materiali e dispositivi utilizzabili come elementi ottici per la lunghezza d'onda Lyman-α. Grazie ad un microscopio a forza atomica (AFM) è stata realizzata una caratterizzazione di tipo morfologico mentra una caratterizzazione ottica ha rivelato le performance di materiali e dispositivi. Le variazioni di tali performance sono state ricondotte a modifiche delle condizioni sperimentali e le conoscenze acquisite sono state utilizzate per ottimizzare le performance del prodotto finito.

L'annealing è un aproccio che non è mai stato completamente esplorato e che può aumentare le qualità ottiche dei film sottili di fluoruro di magnesio, e di conseguenza aumentare la riflettività degli elementi ottici per il range VUV. Io ho condotto uno studio dei fenomeni coinvolti nel processo e applicato la procedura alla realizzazione di migliori specchi per questa regione spettrale. In questo lavoro sono presentati tutti i passaggi sperimentali che hanno condotto alla realizzazione dei dispositivi ultimati e sono descritte le caratteristiche del nuovo approccio dell'annealing.

Ringraziamenti

Desidero ringraziare tutte le persone che mi hanno aiutato a portare a termine questi tre anni di lavoro, a cominciare dai miei supervisori Giampiero Naletto e Maria Guglielmina Pelizzo, e i miei colleghi; Paola e Alain per la guida ed il supporto tecnico e affettivo, Enrico per l'iniziativa e gli slanci di entusiasmo che mi ha garantito dentro e fuori il laboratorio, Francesca per l'empatia e la generosità, e anche Davide, Vanessa, Sara, Lorenzo, Silvia, Alberto e Marcomattia per i momenti e le esperienze condivisi, fondamentali per la mia maturazione e per il felice trascorrimento di questa esperienza. Un ringraziamento anche ad Angelo Giglia per la presenza e gli interventi nei momenti più critici, immancabili nella vita da sincrotrone.

Non credo sia questo il luogo per dilungarmi a ringraziare tutte le persone che, esterne all'ambito accademico, hanno comunque avuto per me un ruolo fondamenetale, sperando di essere stato in grado di renderli consapevoli della loro importanza con le mie azioni. Faccio un'eccezione per i miei genitori, il cui sostegno, critica, amore, è tutto.

Contents

List of Tables

List of Figures

Chapter 1

Ultraviolet light

The term ultraviolet (UV) light refers to electromagnetic radiation with a wavelength ranging from 400 nm to 10 nm, occupying the region of the spectrum between visible light and X-rays. UV radiation is usually invisible to the naked eye, even though under particular condition (for people with aphakia or for very strong illumination) the human eye has some sensitivity up to 310 nm.[1] In nature, some species of insects, birds and fishes can also detect near-UV light.[2]

Very hot objects (over 3000 K) are natural sources of UV radiation, through Black-body emission. The Sun emits ultraviolet radiation at all wavelengths and extremely hot stars emit proportionally more UV radiation than the Sun. Sunlight in space at the top of Earth's atmosphere is, in fact, composed by 50% infrared light, 40% visible light, and 10% ultraviolet light. However, at ground level, percentage of UV light in the solar spectrum is only 3%, since the atmosphere blocks about 77% of the Sun's UV. The UV wavelengths that reach the ground are for more than 95% above 300 nm, while atmosphere blocks most radiation under 320 nm, thanks to the absorption by oxygen molecules and the ozone layer.[3]

Energy from UV radiation, although not great enough to ionize atoms, can break molecular bonds, causing chemical reactions and fluorescence in many substances. Consequently, biological effects of UV are greater than simple heating effects, and many practical applications of UV radiation derive from its interactions with organic molecules. Suntan, freckling and sunburn, not to mention higher risk of skin cancer, are some of the effects of UV light exposure on the human body.[4]

The ultraviolet range of the electromagnetic spectrum, defined most broadly as 10-400 nm, has been subdivided into a number of ranges, depending on its physical behavior or biological interaction, resulting in different classifications, summarized by the ISO standard ISO-21348:

- **UVA** 315-400 nm not absorbed by atmosphere, has physiological effects on organisms;

- **UVB** 290-315 nm partially absorbed by the ozone layer, damaging for living organisms;
- **UVC** 100-290 nm completely absorbed by ozone layer and atmosphere;

- **NUV** 300-400 nm near ultraviolet, light that reach Earth's surface;
- **MUV** 200-300 nm middle ultraviolet;
- **FUV** (o **VUV**) 100-200 nm far ultraviolet (or vacuum ultraviolet), light that needs vacuum to propagate;
- **EUV** 10-100 nm extreme ultraviolet, strongly absorbed by most materials.

The energetic nature of UV radiation has influenced evolution of many animals, including men, and its effects have many implications on human health, both beneficial and dangerous.

The most well-known positive effect of sunlight exposure is the production of vitamin D in the epithelial cells, stimulated by UVB light, which helps to regulate calcium metabolism (vital for the nervous system and bone health), immunity, cell proliferation, insulin secretion, and blood pressure.[5]

Dangerous effects of UV radiation start at 315 nm (limit of UVB band), causing erythema and photokeratitis. This is due to photochemical reactions, which effectiveness is peaked for wavelengths shorter than 275 nm, where skin and eye sensitivity are at their maximum. At these wavelengths though, being radiation strongly absorbed by air, negative effects result limited.

An increased amount of the brown pigment melanin is the natural response of the human body as a protection upon UV exposure. The pigment absorbs UV light dissipating its energy as harmless heat, and as a side effect cause suntan, at different levels according to skin type.[6]

UV's damaging effect on DNA, skin and proteins causes also long term chronical effects, such as skin diseases (rosacea, lupus and others) and skin aging, eye and immune system problems and carcinogen effects.

Not only living being but also organic compounds degrade after UV exposure. Plastics undergo cracking, loss of strength and decoloration, pigments and dyes change colour or fade, making protection from sunlight important for paintings in museums.

1.1 Historical background

The discovery of UV radiation and its properties was a gradual process that spanned three centuries and involved scientists from many countries.[4]

First indirect observations of UV light took place in the XVII and XVIII centuries, when it was discovered that light blackens some compounds, like silver nitrite crystals or silver chloride solution. When directed onto the target through a prism, sunlight showed also to be more effective for the process in the violet end of the spectrum than at the reddish end.

In 1801, Ritter made the hallmark observation. He noticed that invisible rays just beyond the violet end of the spectrum were even more effective at darkening silver chloride-soaked paper. He called them "deoxidizing rays" to emphasize their chemical reactivity and to distinguish them from the "heat rays" at the other end of the visible spectrum. Over time, the simpler term "chemical rays" was adopted. The terms chemical and heat rays remained popular throughout the 19th century, but they were eventually abandoned in favor of the more restrictive terms ultraviolet and infrared radiation, respectively.

Initial studies of the chemical rays focused on their ability to stimulate chemical reactions:

1809 *Gay-Lussac, Thénard.* Concentrated sunlight was capable of converting a mixture of hydrogen and chlorine gases into hydrochloric acid.

1815 *Planché.* Chemical rays darken many kinds of metallic salts.

1826-1837 *Niépce, Daguerre.* Discovery of silver iodide light-sensitivity, beginning of photography.

1842 *Becquerel, Draper.* Photochemical reaction induced by radiation between 340-400 nm, on daguerreotype plate by light after passing a prism. First indication of UV spectral extension.

During the 19th century, research on properties of UV radiation advanced thanks to many contributions:

1802 *Wollaston.* Spectrum seen as a sum of discrete bands.

1814 *Fraunhofer.* Mapping of 500 bands of the solar spectrum.

1859 *Kirchoff, Bunsen.* Invention of the spectroscope demonstrates that different atoms absorb and emit different wavelengths of light. They speculated that the gaps in the solar spectrum are the result of selective absorption by atoms in the Earth's atmosphere.

1865 *Maxwell.* Electromagnetic theory, light is seen as a wave propagating in space generated by interaction of electric and magnetic fields.

1882 *Hertz.* Measuring microwaves reinforce the belief of electromagnetic nature of light.

In parallel with these discoveries, new artificial sources of UV light made their appearance, even if their use was at first limited to their visible emission:

1808 *Davy.* Invention of the open arc lamp with charcoal electrodes attached to a voltaic battery.

1843 *Foucault.* Use of carbon electrodes, more stable but providing dim light.

1877 *Jablochkov, Brush.* Increased power thanks to Gramme dynamo and first useful electric arc lamp.

1898 *Bremer.* Addition of fluoride salts into the carbon electrodes to enhance brightness.

1850 *Stokes.* Use Al electrodes in a quartz tube to produce radiation at 185 nm.

1835 *Wheatstone.* Mercury vapor lamp, bright but prone to deterioration.

1901 *Cooper, Hewitt.* First commercial Hg lamp.

Another significant development in photophysics was the invention of devices for quantifying radiation:

1829 *Nobili.* Invention of thermopile.

1852 *Melloni.* Improvement of the thermopile.

1876 *Crookes.* Invention of rotating vane radiometer.

1878 *Langley.* Invention of bolometer.

Absorption by blackened metal was the physical principle providing light detection for each of the three devices, while they differed in the method used to quantify the signal. The thermopile used a stack of tightly packed metal plates to amplify the photoelectric signal. The radiometer measured light intensity by the number of revolutions induced over time, and the bolometer measured a decrease in electrical resistance upon absorption of radiation. Each provided an effective means of measuring radiation throughout the UV-visible-infrared spectrum.

New discoveries in the field took place in the early years of the 20th century, improving both theoretical and empirical understandings of the behavior of electromagnetic radiation. The most important discoveries concerned quantum nature of light, theorized by Bohr and described as massless particle of energy (named "photons" in 1928 by Lewis) by Einstein. Later on Bohr described interactions between light and atoms as absorption of light from electrons, with consequent reemission at wavelengths that correspond to the electron's energy.

From an experimental point of view, scientists directed their effort to explore the limits of the spectrum. Using prisms or spectrometers placed in vacuum chambers, Schumann, Lyman and Millikan, detected emission of hydrogen at 120 nm and 20 nm, and helium at 50 nm. During these experiments, they found no natural cut-off between UV and X-ray radiation. Studies of UV gas absorption proved oxygen role in absorbing radiation in the UVC region and showed that the Earth's atmosphere reduces UV radiation by approximately 40%, describing solar spectra at Earth surface.

By 1920, the existence of UV radiation, its properties and relationship with sunlight was well established. The potential for commercial and industrial applications shifted the focus to development of new sources (fluorescent lamps, photoflash lamps, stroboscopes, lasers, advanced photon source) and better devices for measuring it (filters, detectors, spectrometers). Research on the interaction of UV radiation with atoms, molecules, solutions and the atmosphere continued. An example of the latter is the work of Molina, Rowland and Crutzen, who have studied the destructive effect of industrial pollutants on the ozone layer. There was also increasing interest in understanding the effects of UV radiation on living organisms, especially humans. The connection between sunlight and UV radiation raised the possibility that many of the effects of sunlight that had been observed over the centuries might be due to these invisible rays.

1.2 Instruments and applications

1.2.1 Sources

There are several types of UV light sources.[7] The most common are the **electric discharge lamps**. These devices are known since the XIX century, and their use is extended to visible illumination, thanks to their greater efficiency and lifetime.

Electric discharge lamps convert electrical energy into light by transforming it into kinetic energy of moving electrons. The primary process is collisional excitation of atoms in a gas to states from which they relax back to the lowest-energy atomic levels by means of the emission of electromagnetic radiation. Three steps compose the process:

1. Free electrons are accelerated by a potential difference which is applied to the device and maintained by an external source of power;

2. The kinetic energy of the electrons is transformed into the internal energy of atomic electron clouds when they collide with atoms, losing kinetic energy in the process;

3. The internal energy of the atoms is dissipated as radiation as the atoms relax back to their lowest energy states. The free electrons are then accelerated again by the external potential and the whole process is repeated.

The radiation emitted by a discharge in a particular gas consists predominantly of a discrete set of frequencies, which are characteristic of the distribution of the permitted energy levels of the atoms constituting the gas.

A second kind of electron collision process that results in radiation is the deflection of an electron by a close encounter with another charged particle, such as another electron, ion or atomic nucleus. Deflection implies, in fact, acceleration and, as described by electromagnetic theory, the acceleration of a charged particle results in radiation. In contrast to atomic radiation, this process brings to a broad distribution of frequencies, since the deflection angle, and hence the resulting acceleration, is not quantized. This process is called Brehmsstrahlung emission.

To produce intense light output is necessary to have a high concentration of free electrons, in order to maximize the collisional excitation of gas atoms. To contain this number of electrons and nullify their repulsion, an equal number of positive ions is necessary. The very process that provides the free electrons simultaneously produces the positive ions; the same collision process that produces the excitation of atomic electron clouds can also result in the ejection of a free electron from an atom, leaving a positively charged remnant ion. This mixture of electrons and positive ions (plasma) is generally contained inside gas-filled glass tubes and are created by the passage through the gas of current injected or extracted by electrodes.

The unique advantage of the atomic radiation from a discharge is that by a suitable choice of atoms composing the gas, the intensity of radiation in a desired frequency band can be made to approach that of the black body (the theoretical upper limit) but be small or zero everywhere else, making it extremely efficient. At the same time, the use of gas instead of liquid or solid allows higher temperatures, resulting in a brighter emission. According to the gas used this type of lamp can emit different spectra, the most common gas, but not the only ones, are mercury-vapor, xenon, deuterium, mercury-xenon, metal-halide. Fig 1.1 shows the spectra of the most common lamps.

When long wavelength radiation or visible light are the targets, the inner wall of an electric discharge lamp is coated with a phosphor that absorbs the UV light produced in the bulb and re-emits it at lower wavelengths by fluorescence. Emission

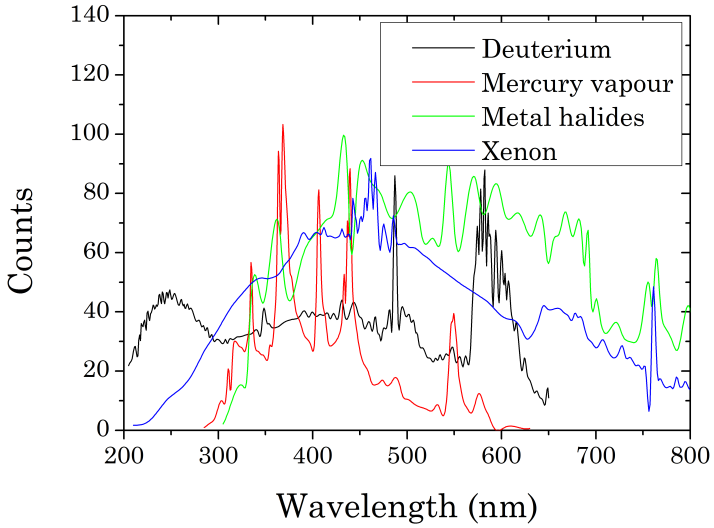

Figure 1.1. Spectra of various gas discharge lamps

can occur in the visible range (**fluorescent lamp**) or in the UVA (**black lights**). Black light lamps emit long-wave UVA radiation and little visible light. Some lamps use a deep-bluish-purple Wood's glass optical filter that blocks almost all visible light with wavelengths longer than 400 nm. Others use plain glass instead of the more expensive Wood's glass, so they appear light-blue to the eye when operating. Mercury-vapor black lights are used for theatrical and concert displays. UVA/UVB emitting bulbs are also sold for other special purposes, such as tanning lamps and reptile keeping.

A shortwave UV lamp can be made using a fluorescent lamp tube with no phosphor coating. A standard mercury lamp of this type produce 85 to 90% of its UV radiation at 253.7 nm. These "germicidal" lamps are used extensively for disinfection of surfaces in laboratories and food processing industries, and for disinfecting water supplies.

Specialized UV gas-discharge lamps containing different gases produce UV light at particular spectral lines for scientific purposes. Argon and deuterium arc lamps are often used as stable sources, either windowless or with various windows such as magnesium fluoride.[8] These are often the light sources in UV spectroscopy equipment for chemical analysis.

The excimer lamp, a UV light source developed within the last two decades, is seeing increasing use in scientific fields. It has the advantages of high-intensity, high efficiency, and operation at a variety of wavelength bands into the vacuum ultraviolet.

Light-emitting diodes (**LEDs**) can emit light in the ultraviolet range, although practical LED arrays are very limited below 365nm, because efficiency and power

output below this wavelength are very poor. Such LED arrays are beginning to be used for UV curing applications, and are already successful in digital print applications and inert UV curing environments.

Many types of **lasers** emit in the UV (gas lasers, laser diodes, solid-state lasers), covering all range. Nitrogen gas lasers, excimer lasers and diode lasers provide radiation at different wavelength between 126 nm (lower limit for Ar_2^* excimer laser) and the visible limit. They found application in industry (laser engraving), medicine (dermatology, and keratectomy), chemistry (MALDI), free air secure communications, computing (optical storage) and manufacture of integrated circuits.

1.2.2 Detectors

Detection of UV photons is based on their ability to excite electrons, creating an electron-hole pair in a semiconductor or current emission through photoelectric effect. Photoelectric effect was discovered in 1887 by Hertz and it consists in an energy transfer from a photon impinging on a metal surface, to an electron of the material, which is emitted from the surface. The effect appears only if electron energy is greater than a certain threshold, the value of which depends on the work function of the material.[9]

A **photocathode** is a negatively charged electrode. When a quantum of light (photon) strikes on its surface, the absorbed energy causes electron emission due to the photoelectric effect. For many years, the photocathode was the only practical method for converting light to an electron current. To operate, the photocathode must be in a vacuum environment, coupled with a positive anode, which collects emitted electrons and allow the current flow. The emitting surface of the photocathode is coated with particular compounds, which work function is tuned to select different operational range. Cs-Te and Cs-I, for example, are sensitive in the UV but visible blind, while other compounds can extend sensitivity until the infrared region.[10]

Nowadays, development of other devices has reduced the use of photocathodes, but they still find an important role in **PhotoMultiplier Tubes (PMT)**. Photomultipliers are extremely sensitive detectors of light in the ultraviolet, visible, and near-infrared. These detectors can multiply the current produced by incident light up to 100 million times, enabling (for example) individual photons detection when the incident flux of light is very low.

Their structure usually consists in an evacuated glass housing, containing a photocathode, several dynodes, and an anode. Incident photons strike the photocathode material, usually deposited on the rear surface of the entry window of the device. Electrons are then ejected from the surface and directed by a focusing electrode toward the electron multiplier, where electrons are multiplied by the process of secondary emission. The electron multiplier consists of a number of electrodes called

dynodes. Each dynode is held at a more positive potential than the preceding one. The potential operates on electrons accelerating them towards the surface of the dynode at kinetic energies of 100 eV; enough to cause emission of a bunch of secondary electrons. These electrons are in turn accelerated toward the following dynodes. The geometry of the dynode chain allows a cascade to occur with an exponentially-increasing number of electrons being produced at each stage. The last stage is the anode, which collects a sharp current pulse that is easily detectable.[11]

If the material of the electrodes has a high resistance, so that the functions of secondary-emission and voltage-division are merged, a "continuous-dynode" structure is feasible. This concept is applied in (single) **Channel Electron Multiplier (CEM)** or continuous channel multiplier. They consist in a glass funnel coated on the inside with a thin film of semi-conducting material, with negative high voltage applied at the wider input end, and positive voltage near ground at the narrower output end. Electrons emitted at any point are accelerated down the funnel, hitting the surface in other positions before reaching the anode. Another geometry of continuous-dynode electron multiplier constitutes the **MicroChannel Plate (MCP)**. It's a 2-dimensional parallel array of very small continuous-dynode electron multipliers. Each microchannel is usually not funnel shaped but parallel-walled.[12]

When the electronic excitation caused by photons allow passage of electrons in the conduction band of a semiconductor, we talk about inner photoelectric effect. This phenomenon is at the bottom of **photodiodes**' operating principle. A photodiode is a p-n junction or PIN structure. When a photon of sufficient energy strikes the diode, it creates an electron-hole pair. If the absorption occurs in the junction's depletion region, the carriers are led away from the junction by the built-in electric field. This creates a photocurrent that is proportional to light intensity.

To obtain imaging sensors, photodiodes can work in parallel combined in arrays. Such devices take the name of **Active Pixel Sensors (APS)** or **Charged-Coupled Devices (CCD)**.

1.2.3 Applications

Its strong interaction with many materials give UV light ability to cause chemical reaction and excite fluorescence. This allows for many applications:

Photographic films are sensitive to UV radiation. Using special lenses and filters to select the right wavelengths, **UV photography** is possible. This is helpful for medical, scientific, and forensic investigations, in applications as detecting bruising of skin, alterations of documents, or restoration work on paintings.

Use of **dyes** that emit visible light when subjected to UV radiation (fluorescence) is common for many applications; to enhance luminosity under daylight, make whites appear brighter, obtain special effects for artistic and visual purpose, prevent forgery, highlight defects in a broad range of materials.

In the forensic field UV illumination helps to identify body fluids and verify the authenticity of collectibles and art. **Detection of organic materials** helps also to identify deficiency in cleaning and sanitary standards. Reading of faded or illegible ink is possible under illumination with different spectral region. This allow access to ancient or damaged documents.

In **chemistry**, UV/Vis spectroscopy is a useful tool to investigate chemical structures and detect dangerous emissions.

Fires emit UV radiation; UV detectors can therefore be used for **fire detection**.

UV light provides fast and low emissions **curing process** for polymers, causing hardening of the polymeric film in a few seconds, for electronic components, optical fibers, glass and plastic bonding, fingernail gels and many others. Modification of polymer's surface in terms of roughness, hydrophobicity and surface energy is also possible thanks to UV irradiation.

UVC (at 184 or 254 nm usually) on titanium dioxide starts a catalytic reaction that oxidize most organic compounds, converting pathogens like pollens, spores and other contaminants, in harmless byproducts. This provide an **air purification** mechanism for indoor environment.

Effectiveness of radiation at 254 nm in damaging DNA of microorganisms, allows for use of mercury-vapor lamps in **disinfection** and **sterilization** in biology laboratories, medical facilities and water treatment.

Ultraviolet radiation is helpful in the **treatment of skin conditions** such as psoriasis and vitiligo.

Effects of UV lights in nature are various and fascinating. Some animals, including birds, reptiles, and insects such as bees, can see near-ultraviolet light. Many fruits, flowers, and seeds stand out more strongly from the background in ultraviolet wavelengths as compared to human color vision. Many birds have patterns in their plumage that are invisible at usual wavelengths but observable in ultraviolet, and the urine and other secretions of some animals, including dogs, cats, and human beings, is much easier to spot with ultraviolet. Pest control technicians can detect urine trails of rodents for proper treatment of infested dwellings.

Butterflies use ultraviolet as a communication system for sex recognition and mating behavior.

Many insects use the ultraviolet wavelength emissions from celestial objects as references for flight navigation. A local ultraviolet emitter will normally disrupt the navigation process and will eventually attract the flying insect. Ultraviolet **traps** called bug zappers use this effect to eliminate various small flying insects.

1.3 Vacuum UltraViolet

The vacuum ultraviolet region extends in the region of the UV spectrum with short wavelengths, from about 200 nm to 100 nm. This region characterize itself for its interaction with matter, resulting from the transitions of the outer electrons of atoms and ions.

Victor Schumann was the first to start exploration into the VUV in 1893, by discovering and overcoming the three obstacles to the extension of spectroscopy below 200 nm:

- The opacity of quartz prisms and lenses, which he replaced by optical elements made of fluorite;
- The lack of transparency of air (due to oxygen) below 185 nm;
- The high absorption of the gelatin on photographic plates.

The second fundamental step was the introduction of the concave grating as the dispersing element, by Lyman, that permitted measurement below the limit of transparency of fluorite (115 nm) down to the region of 25 nm. Use of grazing incident monochromators allowed exploration of EUV until the X-ray limit.

Progresses of VUV research and instrumentation was possible in the XIX century thanks to several technical improvements, in fields as vacuum techniques, grating production and setup, measurement techniques. New instrumentation was produced, to obtain more intense and continuous spectra with new light sources, to improve the quality of fluoride materials and increase reflectivity thanks to appropriate coatings, to develop solar blind and windowless photomultiplier.[13]

1.3.1 Applications

The scientific reasons that encouraged research in this field are development of space **astrophysics** and emergence of plasma research in the period following World War II. With the construction of rockets and satellite able to rise above the atmosphere, the radiation emitted by high-ionized particles became an important source of information about celestial emitters and interstellar matter. Measurement in the VUV can in fact discern chemical composition and temperature of interstellar medium and stars.

To understand these new phenomena, studies of plasma source became necessary in order to obtain "hot" sources with VUV emissions apt to simulate natural radiations. **Study of plasma** characteristics and parameters became an important field of study, intertwined with astrophysics.

In **molecular physics**, electronic transitions to excited states result in a variety of VUV spectra. Analysis of these spectra is often the only way to obtain information

about excited states geometry, which can be very different with respect to the ground state, and is essential for the comprehension of photochemical or high temperature reactions.

Study of ionization properties require also illumination with VUV light, to obtain emission of photoelectrons, which energy spectrum give information on bonds ionization potentials, structure of the ions and presence of substituents, etc.

In **solid-state physics**, the study of the mechanisms of excitation allow construction of band diagrams and characterization of the electronic properties of solids, linked to their optical properties through the relationships between optical constant and dielectric constant. In this wavelength range, light can interact with solids through different processes, like interband transitions, excitonic transitions and plasmonic oscillations.

Determination of optical constants in the VUV is a task made complex by several difficulties, like the impossibility of transmittance measurement, due to little transparency of materials, the sensitivity to internal structure and defects, the great influence of surface roughness and cleanliness.[13]

Another type of spectroscopy where VUV has application is **circular dichroism (CD) spectroscopy**. Circular dichroism (CD) is the difference in the absorption of left-handed circularly polarized light (L-CPL) and right-handed circularly polarized light (R-CPL). It occurs when a molecule contains one or more chiral chromophores (light-absorbing groups). Its importance is linked to its ability to study large biological molecules.

The secondary structure or conformation of macromolecules, particularly proteins, is sensitive to its environment, temperature or pH. Circular dichroism can be used to observe how that structure changes with environmental conditions or on interaction with other molecules, obtaining structural, kinetic and thermodynamic information about them.[14]

A more technical application for VUV light is **photolithography**, where light, after passing through a mask, causes a chemical reaction in selected areas of a material called photoresist. The reaction causes solidification of the photoresist, while the shadowed parts can be washed away. In this way is possible to "etch" away, deposit on or otherwise modify areas of the sample where no photoresist remains. The process plays an important role in the semiconductor industry, allowing fabrication of integrated circuits and printed circuits boards. The standard wavelength used to fabricate electronic devices is 193 nm. Experimental extreme ultraviolet lithography uses wavelength as short as 13.5 nm instead.[15]

The **electro-optics** field (also called photonics) offers new and interesting applications in the VUV. This field, a branch of electrical engineering and material physics, concerns the interaction between the electromagnetic (optical) and the electrical (electronic) states of materials. It involves components, devices (e.g. lasers,

LEDs, waveguides etc.) and systems which operate by the propagation and interaction of light with various tailored materials.[16]

1.3.2 Instruments

This range often requires specific instrumentation. To avoid absorption from air, setups call for vacuum chambers or pure nitrogen atmosphere, the second being simpler and cheaper but useful only between 150 and 200 nm. Detectors are often solar blind, because sources in this range are weak if compared to visible radiation. Specific lamps are required.

Sources

Since the main emission peak for mercury lamps is at 253.7 nm, to obtain a gas discharge lamp in the VUV different gases are necessary. Deuterium it's the main choice, it produces a continuous spectrum in the VUV, peaked at 121.6 nm, and comparatively little output in the visible and infrared. **Deuterium lamps** are low-pressure gas-discharge light source. Use of common hydrogen instead of deuterium provides a weaker emission at the far end of the UV range and shorter life spans, but is far less expensive. Fig. 1.2 shows the typical spectrum of a deuterium lamp.

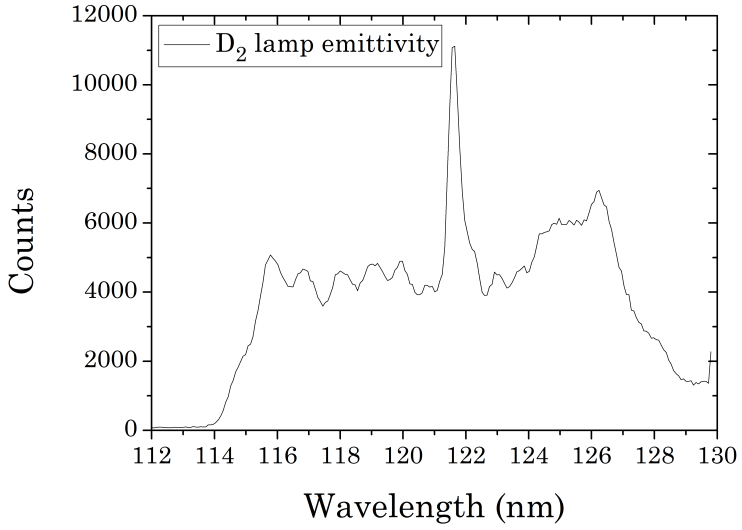

Figure 1.2. Deuterium lamp spectrum

The **hollow-cathode lamp** (HCL) is a spectral line source used for discrete wavelength emission in spectrometers and for laser tuning. This lamp is composed by a cathode, an anode and a buffer gas. A large voltage between anode and cathode ionize the gas, creating the plasma. Noble gases are the best choices. Ionized gas

atoms are accelerated towards the cathode, causing sputtering. Relaxation of both gas atoms and sputtered materials causes emission.

To tune with a HCL a light source, the source is placed behind the HCL and the radiation emitted from the source conducted through the lamp. When the emission wavelength corresponds to the correct electronic transition, it excites electrons in the gas causing an increase in current that indicates the correct tuning of the source.

The need for high intensity sources at shorter and shorter wavelengths found an important aid in **synchrotron light sources**. Synchrotron radiation is produced in storage rings, particle accelerators and synchrotrons. In these facilities, electrons are accelerated to relativistic speeds, and forced in a closed path by magnetic fields. Accelerated particles (usually electrons) lose energy emitting light, and relativistic effects move emission towards shorter wavelengths and collimate emitted radiation on the ring plane. As a result, synchrotron radiation sources are by far the most brilliant in X-rays and FUV. The advantages of this techniques are so relevant that, if at the beginning synchrotron radiation was used in "parasitic mode" from facilities dedicated to particle acceleration studies, now storage rings are built specifically as light sources. Bending magnets and insertion devices (undulators and wigglers) are inserted in the structure to maximize the brilliance and give emission in a wide range from X-rays to UV. The major applications of synchrotron light are in condensed matter physics, materials science, biology and medicine.[17]

Lasers have been used to indirectly generate non-coherent extreme UV (EUV) light. The EUV light is not emitted by the laser, but rather by electron transitions in an extremely hot tin or xenon plasma, which is excited by an excimer laser. This technique does not require a synchrotron, yet can produce UV at the edge of the X-ray spectrum.

Detectors

Photon detection in the VUV is possible thanks to a variety of detectors with useful response and sensitivity. Even though there are limitations due to low intensities in this region and low efficiency of optical elements and windows, there are detectors with single photon counting sensitivity and imaging capabilities. Exception made for those envisaging photo-ionization of gases, the base principles are the same as visible and infrared sensors: surface photoemission, electron-hole pair creation or chemical reactions in photographic emulsions.[18]

Photographic plates are used in the VUV for their high spatial resolution (of about 1 μm), in spectroscopic measurements and high-resolution wavelength measurements. They have the disadvantage of a nonlinear response and a limited dynamic range. Since gelatins for photographic emulsion absorb in the VUV, special plates are used for this range.

PMT and **CEMs** have low dark count and single-photon sensitivity and are

used for photon counting, nonimaging applications. Coatings for the photocathode like CsI, KBr or alkai halides, grant a 15-20% efficiency in the VUV, while cutting radiation above 150-300 nm, giving minimal response to stray ambient light. In the shorter wavelength region, where there are no optical window material, bare PMTs can be used, but exposure to air causes coating degradation and metal surfaces like tungsten or aluminum must be used. Sodium salicylate and other compounds offer the possibility to convert VUV in visible light thanks to fluorescence.

Vacuum photodiodes are used as radiometric transfer-standard detector in the whole VUV range, thanks to their stability and spatial uniformity. These devices do not have an amplifying system and the sensitivity is lower, signals of 106 photons/s are necessary.

Use of silicon photodiodes is limited by absorption of the oxide layer and sensitivity to longer wavelengths. Thinning of the oxide region and development of non-silicon wide band gap devices (GaN) led to an increase in the use of these devices. Thin films filters can also reduce stray light sensitivity of these instruments.

MCPs combine single photon sensitivity with spatial resolution (10-25 μm). Quantum efficiency is 20%. The position of the incoming photon is determined by direct detection of the resulting electron cloud or by conversion in visible light through a phosphor.

For **CCDs** to work in this wavelength range absorption from gate and passivation layer must be limited. To do so, overcoating with a phosphor to increase wavelength, or back illumination of a thinned and surface-treated CCD are possible. Sensitivities are comparable to those of MCPs. The latter are preferred for low light-level imaging, while the former are used with higher level of illumination.

Another mean of photon detection in this region is the use of **ionization chambers**. In these chambers, impact of photons with gas atoms or molecules causes an ionization that can be collected when an appropriate voltage is applied. Efficiency approach 100% over the ionization threshold and individual photon detection is possible. Since chambers works with high gas pressure (100-2000 torr) they cannot be used in the windowless region of the spectrum.

Optical elements

Optical elements working in the VUV range suffer from constrains dictated by the performances of optical materials in terms of reflection and transmission.

Spectrometers and monochromators in the VUV are concave normal incidence **gratings**. The concave shape is essential to provide focusing power and eliminating the need for additional mirrors, thus limiting reflection losses. Standard spherical gratings suffer from astigmatism, resulting in loss of signal and resolution. To reduce this problem aspherical (toroidal) mirrors are adopted, which have coincidence between horizontal and vertical focal point. This instruments have a resolving power

of more than 10^5 $\lambda/\delta\lambda$. Normal incidence gratings work from 200 nm to 30 nm, for lower wavelengths reflectance of all standard coatings fall to a few percent. In this region is necessary to use grazing incidence instruments that exploit total reflection. A reflectance cutoff for these instruments limits their use to wavelength above 1 nm. Resolving power of these instruments is generally lower than that of their normal incidents counterparts.

The most evolved gratings make use variable line spacing or interference techniques to produce holographic gratings. Variable spacing reduces periodic irregularities and scattered light, correct for spherical aberration, allow high groove densities and is easily applied to aspheric surfaces.

For high-resolutions, Fourier transform spectroscopy is a viable option. With a resolution of $8.5 \cdot 10^5$ $\lambda/\delta\lambda$ at 140 nm, this technique offers better resolution than the best VUV grating.

Few choices are available for use as windows at wavelengths below 200 nm. The most common choices are fused quartz (160 nm), sapphire (145 nm), CaF_2 (125 nm), MgF_2 (115 nm), LiF (105 nm). Between brackets their lower limit is shown. Under 105 nm there are no transparent materials.

An alternative to windows in this region is the use of capillaries, slits or circular apertures to separate differentially pumped regions. Typical dimensions are 10-100 μm diameter apertures with 3 mm length. Optical transmittance of these elements is between 20% and 50%, a compromise between optical loss and gas conductance is required.

For **reflective coating** in the VUV MgF_2 coated aluminum layers provide reflection of 80-85%. Under 100 nm normal incidence reflectivity drops for all materials to values not superior to 15-30%, common material choices are Os, Pt, Au, and Ir.

Use of **interference filters** is limited by lack of coating materials with sufficient transmission and suitable optical constants coupling. Dielectric reflectors thus have a great number of layers. Even so, these devices can provide reflection and narrow filtering at short wavelengths.

Chapter 2

VUV and astrophysics

As already outlined in the previous chapter, study and development of instrumentation in the VUV range has been deeply connected with the field of astrophysics. The Sun, along with other interstellar emitters, is a source of radiation in the 100-200 nm range. The study of its spectra can reveal much information about chemical composition, temperatures and dynamics. In this context, the 121.6 nm wavelength spectral line is particularly interesting. At this wavelength, in fact, take place the Lyman-α emission of hydrogen, and the analysis of such radiation gives information about temperature and densities of this element in the upper solar chromosphere and low solar transition region.

2.1 History of solar exploration

Our star is, of course, the body of the solar system that is most influential for life, environment and dynamics on Earth. For this reason it was one of the favorite targets since the early stages of space conquest. Several mission have been dedicated to the study of our star, and the list lengthen considerably if one consider also mission dedicated to the study of solar effects on Earth's atmosphere.[19]

In 1960, the launch of the **Pioneer 5** spacecraft began a long series of missions dedicated to the understanding of the solar environment. This probe, a spin-stabilized sphere with a 0.66 m diameter, had on board four instruments, which collected data on solar particles and radiation (photons with E $>$ 75 MeV and electrons), intensity of magnetic field at the geomagnetic boundary and in interplanetary space, cosmic ray radiation and amount of meteoric dust particles and their momentum. For a period of more than one month the probe returned information on flare particles and cosmic radiation and measured the magnetic field, while the micrometeorite counter failed to operate.[20]

The success of this first mission was shortly followed by a series of missions

launched between 1965 and 1968, the **Pioneers 6, 7, 8, 9**. These spacecrafts were designed to provide continuative measurement of interplanetary phenomena from different points in space. The crafts were identical, spin stabilized cylinders of 0.94 m diameter and 0.81 m height powered by solar cells and battery, orbiting around the Sun. They provided detailed measurement of solar wind (electrons and cations), solar magnetic field and cosmic rays. Data were used to understand stellar processes, dynamics of solar wind and solar weather. These missions were successful and long-lived. Although the spacecraft have not been recently used for data collection, contact is still possible with spacecraft 6, 7 and 8. Since the first launch in 1965 to the last contact in 2000, the Pioneer 6 operated continuously for 35 years, when its original life expectancy was only six months.[21]

Another program, the Orbiting Solar Observatory (**OSO**), launched between 1962 and 1975, in parallel with the Pioneers, 8 satellites designed to study an 11-year sun spot cycle in UV and X-ray spectra. They observed solar flares, measured background X-ray radiation from 14 to 200 keV and emission of γ-rays not only from the Sun but also from other stars and galaxies.

The first study of solar electromagnetic emission was carried out with the Apollo Telescope Mount (**ATM**), on board of the first American space station, Skylab. From 1973 to 1974 the astronauts of the space station manually operated ATM, providing imaging and spectroscopic data at various wavelengths. Data were impressed on photographic films and returned to Earth with the crew. The eight instruments on board of the ATM allowed observation of radiation from 0.2 to 700 nm, with X-ray and VUV telescopes, a visible coronagraph, and spectrometers in the UV and EUV regions.[22]

Shortly after, a joint venture between West Germany and NASA launched two spacecraft, **Helios-A** and **Helios-B** (also known as Helios 1 and Helios 2), into a heliocentric orbit with the purpose of studying solar processes. The first probe was launched in 1974, followed two years later by the second, which flew closer to the Sun, having a perihelion of 0.29 AU. Until 1985 they provided data with 8 instruments, measuring velocity and distribution of the solar wind plasma, strength and direction of solar magnetic field, distribution of cosmic rays, composition and dynamics of interplanetary dust particles and their scattering effect on sunlight.

The Solar Maximum Mission (**SMM**) satellite, launched in 1980, focused its research on solar flares and worked until 1989, when reentered the atmosphere, burning up. The satellite studied solar eruptions with a coronagraph coupled with spectrometers and imagers in the UV, X-ray and γ-ray. Between its discoveries, the mission shown that, contrary to the expectations, the Sun is brighter during the sunspot maximum, because feculae, which surround the darker sunspots, are so bright that they more than compensate the darkening effect of the spots. The mission discovered also ten sungrazing comets.

In 1990, a new mission, born thanks to the collaboration between NASA and

ESA, provided a new study of the Sun thanks to its particular orbit, well outside the plane of the Solar System. The space probe **Ulysses**, reached in fact, thanks to gravity assist from Jupiter, an orbital inclination of 80° and could study the Sun's poles. The spacecraft was a spin-stabilized box of size 3.2×3.3×2.1 m. The complex path of the spacecraft, which brought it near the Sun after reaching long distances from the star, caused some technological difficulties. Power could not be provided by solar cells, so a radioisotope thermoelectric generator was necessary. Shielding from both heat and cold was included in the design. The instruments on board were radio and plasma antennas, X-ray detector, magnetometer, detectors for electrons, ions, neutral gas, dust, and cosmic rays. This was the first mission to exploit gravity assist to exit the ecliptic plane. Thanks to its innovative orbit it could study the solar poles, solar wind, Jupiter environment, several comets and γ-ray bursts. The power allowed it to explore the polar areas for three passages, before shutdown in 2009. The scientific discoveries were many and important. It found a complex interaction between magnetic field and Solar System, discovered an amount of dust coming from deep space 30 times more abundant than expected and a magnetic field at the poles weaker than foreseen, measured a weakening of the solar wind with time. It was also a part of a network for triangulation of γ-ray bursts.

In 1991, a Japanese solar observatory spacecraft, **Yohkoh**, started its observations. It worked on a near-circular orbit around Earth, three-axes stabilized, carrying four instruments: a Soft X-ray Telescope, a Hard X-ray Telescope, a Bragg Crystal Spectrometer and a Wide Band Spectrometer. Utilizing a CCD as its readout device, perhaps being the first X-ray astronomical telescope to do so, it could reveal an interesting and extensive amount of data about the behavior of the solar corona. Previous solar soft X-ray observations, such as those of Skylab, had been restricted to film as a readout device. Yohkoh therefore returned many novel scientific results, especially regarding solar flares and other forms of magnetic activity.

NASA returned to solar study with the Solar Anomalous and Magnetospheric Particle Explorer (**SAMPEX**), first mission of the Small Explorer program. The spacecraft, in low Earth orbit since 1992, measured, until 2004, anomalous components of cosmic rays, emissions from solar energetic particles, and electron counts in Earth's magnetosphere. Its instruments were the Heavy Ion Large Telescope (HILT), the Low Energy Ion Composition Analyzer (LEICA), a Mass Spectrometer Telescope (MAST) and the Proton/Electron Telescope (PET).[23]

An important and long lasting mission is the ESA NASA joint project that put the spacecraft Solar and Heliospheric Observatory (**SOHO**) in orbit around the lagrangian point L_1. From 1995, it continues to collect data and images of the Sun. The three main scientific objectives of SOHO are: investigation of the outer layer of the Sun (chromosphere, transition region, and the corona), observations of solar wind and associated phenomena in the vicinity of L_1, probing the interior structure

of the Sun. SOHO's data are also used for solar weather forecast, and to predict coronal mass ejection (CME) arrival times at earth, so electrical grids and satellites can be protected from their damaging effects. Another side effect of SOHO's activity is the discovery of Sun grazing comets, up to date the number of discovered comets is greater than 3000. The payload consists of 12 instruments, Coronal Diagnostic Spectrometer (CDS) which measures density, temperature and flows in the corona, Charge ELement and Isotope Analysis System (CELIAS) which studies the ion composition of the solar wind, Comprehensive SupraThermal and Energetic Particle analyser collaboration (COSTEP) which studies the ion and electron composition of the solar wind, Extreme ultraviolet Imaging Telescope (EIT) which studies the low coronal structure and activity, Energetic and Relativistic Nuclei and Electron experiment (ERNE) which studies the ion and electron composition of the solar wind, Global Oscillations at Low Frequencies (GOLF) which measures velocity variations of the whole solar disk to explore the core of the Sun, Large Angle and Spectrometric Coronagraph (LASCO) which studies the structure and evolution of the corona by creating an artificial solar eclipse, Michelson Doppler Imager (MDI) which measures velocity and magnetic fields in the photosphere to learn about the convection zone which forms the outer layer of the interior of the Sun and about the magnetic fields which control the structure of the corona, Solar Ultraviolet Measurement of Emitted Radiation (SUMER) which measures plasma flows, temperature and density in the corona, Solar Wind ANisotropies (SWAN) which uses telescopes sensitive to a characteristic wavelength of hydrogen to measure the solar wind mass flux, map the density of the heliosphere, and observe the large-scale structure of the solar wind streams, UltraViolet Coronagraph Spectrometer (UVCS) which measures density and temperature in the corona, Variability of solar IRradiance and Gravity Oscillations (VIRGO) which measures oscillations and solar constant both of the whole solar disk and at low resolution, again exploring the core of the Sun. Many of the images provided by the spacecraft are of public domain and offer great views of the Sun, in various range of wavelength.

Together with SOHO at the Lagrangian point, there is, from the 1997, the Advanced Composition Explorer (**ACE**), a spacecraft dedicated to energy particles detection. Its scientific objectives are: evaluation of elemental and isotopic composition of matter; study on origin of the elements and subsequent evolutionary processing; investigation on the formation of the solar corona and acceleration of the solar wind; analysis of particle acceleration and transport. It has a payload comprising a variety of instruments: Cosmic Ray Isotope Spectrometer (CRIS), Solar Isotope Spectrometer (SIS), Ultra Low Energy Isotope Spectrometer (ULEIS), Solar Energetic Particle Ionic Charge Analyzer (SEPICA), Solar Wind Ions Mass Spectrometer (SWIMS), Solar Wind Ion Composition Spectrometer (SWICS), Electron, Proton, and Alpha-particle Monitor (EPAM), Solar Wind Electron, Proton and Alpha Monitor (SWEPAM), Magnetometer (MAG), Real Time Solar Wind (RTSW).

ACE observed the particles of the solar wind, particularly those at higher energy, like supratermal solar wind particles; analysed the corotating interaction regions (CIR), shock waves formed by the collision of wind streams at different velocities; and also studied the energetic particles due to CMEs and flares and anomalous cosmic rays.

In 1998, NASA launched a heliophysics and solar observatory, the Transition Region and Coronal Explorer (**TRACE**), to obtain high resolution images of solar photosphere and the transition region to the corona. The data were used to correlate the magnetic field to plasma structures on the Sun. a particular focus for the instrument was the study of fine structure on coronal loops. The telescope worked until 2010.

The mission **Genesis**, 2001, was the first mission after the Apollo program to return space samples to the Earth. The probe crashed upon landing because of a flow in the parachute design, contaminating most of the samples. Despite this, many samples were collected and the contamination removed, achieving successfully all the major scientific objectives. The 3 main objectives were: to obtain precise solar isotopic abundances of ions in the solar wind, as essentially no data having a precision sufficient for solving planetary science problems were available; to obtain greatly improved solar elemental abundances by factor of 3-10 in accuracy over what the literature; to provide a reservoir of solar matter for 21st century science to be archived. The collection of solar wind ions occurred by implantation of the ions under the surface of the collectors, while they were facing the Sun for all the length of the mission. Other array of detectors were deployed only in presence of determinate situations (CME, fast or slow wind), to verify the maintenance of composition proportions throughout the processes which form the solar wind. A third type of collector, the concentrator, focused light ions onto a small target, to study isotopic composition. Among the discoveries of this mission, a higher proportion of ^{16}O than on Earth was found and study of argon and neon isotopes discounted some theoretical models of stellar genesis.

The Reuven Ramaty High Energy Solar Spectroscopic Imager (**RHESSI**) studies, since 2002, energy release and particle acceleration in solar flares. Its instrument can detect high energy photons, from soft X-rays ($\sim$3 keV) to gamma rays (up to $\sim$20 MeV), performing imaging and spatially resolved high resolution spectroscopy. Photons of such energies are released during flares due to acceleration of electrons (X-rays) and cations (γ-rays); the instrument provided important information on position and amount of energy release in the solar atmosphere, allowing a better understanding of the mechanisms at the bottom of high energy acceleration, a process that has important consequences not only for solar physics but also for magnetospheres and active galaxies.[24]

The Yohkoh mission had a follow-up in the mission **Hinode**, realized in collaboration with USA and UK in the 2006. The probe, from a sun-synchronous orbit around Earth, explore the solar magnetic field and its interaction with the corona.

With 3 instruments: a Solar Optical Telescope (SOT), an X-ray Telescope (XRT) and a Extreme-Ultraviolet Imaging Spectrometer (EIS) it studies the mechanisms that power the solar atmosphere and drive solar eruption.[25]

In the same year another mission allowed for the first time 3D observation of the Sun. The Solar Terrestrial Relations Observatory (**STEREO**) consists of two identical spacecraft orbiting the Sun in opposite directions, separating from each other at a rate of approximately 44° per year. In 2011 their separation was of 180°, allowing imaging of the entire Sun. At the moment the spacecrafts are on the opposite side of the Sun with respect to the Earth and contact is lost, maybe permanently. The main benefit of this mission was the ability to monitor the Sun from different positions, allowing stereoscopic imaging and monitoring of the far side. This was mainly used to improve forecast on CMEs, knowledge in solar physics and to discover binaries systems. The instruments have on board five cameras: an EUV imager, two coronagraphs and two imagers pointed at the space between earth and Sun; they are to follow the path of CMEs throughout their journey. The instrument IMPACT studies energetic particles, PLASTIC studies plasma characteristics of solar wind, SWAVES studies radio disturbances traveling from Sun to Earth.

From 2010 the Solar Dynamics Observatory (**SDO**), by NASA, is observing the Sun, studying generation and structure of the solar magnetic field, mechanisms of solar wind formation and variation of solar irradiance. The goal is to provide imaging at small scales in space and time and at various wavelengths of the solar atmosphere, to understand its influence on Earth. There are on board 3 instruments, a Helioseismic and Magnetic Imager that analyzes the solar interior, its magnetic field and its variability, the Extreme Ultraviolet Variability Experiment (EVE) that monitors Sun's extreme ultraviolet irradiance, and the Atmospheric Imaging Assembly (AIA) that observes chromosphere and corona at seven different wavelengths in the EUV. This mission provides with respect to the previous ones a better resolution and imaging quality. SDO works on a circular geosynchronous orbit.

At this time the last satellite launched for solar observation was the Interface Region Imaging Spectrograph (**IRIS**), in 2010, that studies the chromosphere of the Sun, thanks to an ultraviolet telescope combined with a spectrometer. The results it achieved have an unprecedented detail and resolution, allowing discovery of new features like solar heat bombs, high-speed plasma jets, nano-flares, and mini-tornadoes, describing a complex and greatly changing environment in terms of temperature and density changes. Such high resolution will serve as a microscope for larger instruments that capture images of the whole sun simultaneously (e.g. SDO). It operates from a polar sun-synchronous orbit.

2.2 Lyman-α observations

The missions listed in section 2.1 operated with various techniques and instruments to investigate different areas and processes of the Sun. Of interest for this work are those instruments dedicated to analysis of the VUV emission of the hottest region of the Sun. In particular the study of light emitted by hydrogen at 121.6 nm and of the optical elements necessary for its detection is the most relevant in the following.

The transition of an electron from the electronic state with n=2 to the ground state (n=1) causes emission of a photon. For hydrogen the wavelength of the emitted radiation is 121.567 nm, a spectral line called Lyman-α (Ly-α). In the solar chromosfere and corona, due to composition and high temperatures of the matter constituting our star, there is abundance of excited hydrogen atoms. This results in an observable emission at that wavelength, that can be useful to understand dynamics, temperatures, densities and processes happening on the surface of the star. This was clear since the beginning of space exploration, in fact, already in the first missions, like OSO and the Skylab station, there were instrument dedicated to such purpose.

The **ATM**, the Skylab module dedicated to solar observation, carried an ensemble of six instruments that covered a range from 0.2 to 700 nm, spanning from soft X-rays to UV and visible light. Operating in the VUV portion of the spectrum were two instruments, a former operated from 30 to 140 nm, performing digital scans of selected section of the Sun in monochromatic light, at seven wavelengths simultaneously. The lines chosen for the analysis were distinctive of different temperature region in the solar atmosphere. The latter operated between 97 and 394 nm. The instruments studied chromospheres, transition region and also lower corona. Recording of data was made with photographic films.[26]

Sounding rocket were cheap missions, useful for both obtaining data and experimenting new technologies and techniques, to be applied in following missions. They involved the launch of a rocket in a parabolic flight, with a few minute of time dedicated to measurement at the top of the trajectory, possibility of retrieving the payload at the end of the flight, and with the advantage of avoiding all the costs e complexity of putting a satellite in a stable orbit. In 1979, for example, a mission that had this characteristics took place. On a Black Brant rocket, a Transition Region Camera (**TRC**) took 1" resolution pictures at Ly-α which presented structures never seen before. The TRC was a Cassegrain telescope, with Al/LiF mirrors and two interference filters in series to isolate the L-α line from the background. It showed, on photography film, very detailed photograph of the Sun's surface, with bright active spot in evidence, connected by characteristic loop structures.[27]

The Multi-spectral solar telescope array (**MSSTA**), was a sounding rocket payload that constituted the precursor of all the normal incidence EUV telescope in use today, being the first to mount normal incidence reflective multilayer optics. It flew

3 times, in 1991, 1994 and 2002 and it had on board 10 different telescopes working in parallel in different wavelength ranges. In the VUV operated a Ritchey-Chrétien telescope with mirrors coated in $Al/MgF_2/Os$. A MgF_2/Al filter could select the 121.6 nm wavelength with a band pass of 6.5 nm.[28]

This preliminary missions prepared and allowed for the success of SOHO, which is producing a great amount of information thanks to its imaging capabilities. Among the 12 instruments on board, 3 works in the VUV. **SUMER** (Solar Ultraviolet Measurements of Emitted Radiation) is the instrument designed for the investigation of plasma flow characteristics, turbulence and wave motions; plasma densities and temperatures; structures and events associated with solar magnetic activity in the chromosphere, the transition zone and the corona. In those regions, great variations in activity, densities, temperature, features, happen sharply as a function of height and position. To investigate these dynamics, the instrument work as a spectrograph, with SiC coated mirrors and a grating working from 33 to 161 nm. The detectors register the diffraction spectra or, thanks to the rotational capabilities of the primary mirror, monochromatic images of selected areas.[29]

UVCS (UltraViolet Coronagraph Spectrometer) investigates with UV spectroscopy and visible polarimetry the extended solar corona, measuring random velocity distributions, densities and the outflow velocities of particles. Its purpose is the understanding of physical processes controlling the extended solar corona and the generation of the solar wind. The spectrometer is composed by three separate paths that analyze different wavelength (Ly-α, O VI and Vis). The Ly-α channel is a toric grating spectrometer with an entrance slit mechanism, a neutral density filter inserter, a grating mechanism, and a windowed crossed delay line detector. This channel is optimized for line profile measurements of H I 121.6 nm and may also be used for other spectral lines in the 114.5 nm to 128.7 nm spectral range. An extended wavelength range (110 nm to 136.1 nm) may be observed by rotating the grating. The optical elements in this path are coated with Al/MgF_2.[30]

The **SWAN** (Solar Wind Anisotropies) Instrument is designed to observe the solar Ly-α photons backscattered by the neutral hydrogen atoms present in the interplanetary medium. The instrument rotates to collect images of the full-sky, three times per week. The images are then processed to reveal spatial variations of the solar illuminating flux. These spatial variations are correlated to the actual activity on the solar disk. Because SWAN observes backscattered photons, it is actually possible to 'see' those which are originating from the far side of the Sun. The instrument is provided with two sensors, exploring the two hemispheres. Each one works with a hydrogen absorption cell which allows for a fine spectral analysis of the Ly-α line profile. When the H cell is activated on the light path to the detector, dissociating the hydrogen gas molecules present in the cell, it creates a negative filter, which blocks the emission line. The recorded intensity (integral over the line profile) decreases, and the fraction of light which was blocked is called the

absorption factor A and its use to build images of the sky at 121.6 nm.[31]

TRACE (Transition Region and Coronal Explorer) is a space-borne solar telescope featuring high spatial and temporal resolution. TRACE images emission from solar plasmas in three EUV wavelengths and several UV wavelengths, covering selected ion temperatures from 6000 K to 1 MK. The TRACE UV channel employs special optics to collect images of the H I Ly-α line, the C IV resonance doublet at 154.8 and 155 nm, the UV continuum near 155 nm, and also a white-light image covering the spectrum from 200 to 800 nm. It is a Cassegrain telescope divided in four quadrants, three of which are EUV sensitive, while the fourth works from VUV to visible range. The EUV quadrant bandpass selections are determined by multilayer coatings on the primary and secondary mirrors. The UV quadrant employs a selection of broadband and narrowband filters, designed to optimize transmission at both 121.6 and 155 nm and also reject longer wavelengths. The entrance window filter is a single crystal MgF_2 substrate coated with a broadband multilayer metal-dielectric interference coating. The primary mirror is coated with an all-dielectric multilayer interference coating with peak reflection of approximately 83% at 154 nm and a bandwidth of 15 nm FWHM. The reflectivity drops to 10% at 121.6 nm and at wavelengths above 160 nm. The UV quadrant of the secondary mirror is coated with Al/MgF_2. Visible light is excluded from the EUV quadrants by thin Al entrance filters mounted on a nickel mesh. The UV quadrant is shielded by a broadband UV filter. A quadrant selector located directly behind the entrance filters selects which of the four channels is active.[32]

The Ly-α images produced by TRACE are, however, composed of not only the desired line emission, but also local ultraviolet continuum and longer wavelength contamination. This contamination has frustrated attempts to interpret TRACE observations in H I. The Very Advanced Ultraviolet Telescope (**VAULT**) sounding rocket payload was launched in and dedicated to H I imaging. Combining its observations with that of TRACE it was possible to remove UV continuum and longer wavelength contamination from TRACE Ly-α images. VAULT was a Cassegrain telescope followed by two gratings, coupled to improve the spectral sensitivity to a bandpass of 15 nm. The obtained images were not only useful for interpretation of TRACE data, but also were the highest-resolution images available at the time.[33]

Analysis at Ly-α is helpful not only for solar missions, but also in other environments. The TIMED (Thermosphere Ionosphere Mesosphere Energetics and Dynamics) mission studies the dynamics of the Mesosphere and Lower Thermosphere (MLT) portion of the Earth's atmosphere, the region located between 60-180 km above the Earth's surface where energy from solar radiation is first deposited into the atmosphere. The spacecraft is in orbit since 2001 and it carries two instruments capable of measurements at Ly-α. Solar radiation under 200 nm is completely absorbed in the region of interest, changing the photochemistry, dynamics, and energy balance of

the upper atmosphere. The Solar Extreme Ultraviolet Experiment (**SEE**), measuring the ultraviolet irradiance arising from flares, solar rotation (27 days), or the 11 year solar cycle, links changes in the photochemistry, dynamics, and energy balance of the upper atmosphere with their solar causes. SEE's grating spectrograph scans UV radiation from 27 to 194 nm with resolution of 0.4 nm.[34]

The second instrument, Global Ultraviolet Imager (**GUVI**) is a far-ultraviolet imaging spectrograph designed to globally measure the composition and temperature profiles of the MLT region, as well as its auroral energy inputs. The spectrum received from the detector ranges from 115 to 180 nm. Rotating a mirror in the direction perpendicular to the diffraction plane it is possible to obtain spatial imaging.[35]

Other missions study the solar output and its effects on the atmosphere. Since 2003, the SOlar Radiation and Climate Experiment (SORCE) identify the irradiance from the Sun with a collection of instruments. Data obtained by the SORCE experiment are been used to model the Sun's output and to explain and predict the effect of its radiation on the Earth's atmosphere and climate. In the UV range the instrument **SOLSTICE** works as a spectrometer, collecting data from 115 to 320 nm.[36]

Chapter 3

Solar Orbiter and METIS

The results from all the missions previously described have contributed to our understanding of the solar corona, the solar wind, and the three-dimensional heliosphere. Each of these missions had a specific focus, being part of a strategy of coordinated solar and heliospheric research. However, some pieces of the puzzle are still missing. None of these missions have been able to fully explore the interface region where the solar wind is created with sufficient detail to link solar wind structures back to their source regions at the Sun.

For this reason ESA has programmed and developed the Solar Orbiter mission (SolO). An idea born in 1998 and since then developed and modified to its final form, that should leave the ground in October 2018. The mission will be launched with an Atlas V 411 Evolved Expendable Launch Vehicle (EELV) from the Cape Canaveral air force station in Florida. A voyage of three years will bring it on an orbit with perihelion at 0.28 AU, to observe the Sun at the closest distance ever reached. The spacecraft will observe the Sun during a nominal mission of 7 years (trip included), which can be extended for other 3.

Thanks to its orbit, close and out of the ecliptic, and its wide range of instrumentation, combining in-situ and remote-sensing instruments, it will address the central question of heliophysics: How does the Sun create and control the heliosphere?[37]

3.1 Sun physics, state of the art

Our understanding of the Sun has improved greatly upon the centuries. We now know that the Sun is a nearly perfect spherical ball of hot plasma, with a diameter about 109 times that of Earth (696342±65 km, and with a mass about 330000 times that of Earth ($1.99 \cdot 10^{30}$ kg). About 3/4 of the Sun's mass consists of hydrogen; the rest is mostly helium, with much smaller quantities of heavier elements, including oxygen, carbon, neon and iron.[38]

It is a G-type main-sequence star formed approximately 4.567 billion years ago, with a complex structure at its interior. Its core extends from the center to about 20-25% of the solar radius ($R_\odot$), with high density (about 150 times the density of water) and temperature (15.7 MK). Sun's energy is produced by nuclear fusion in this region. From the core out to about 0.7 $R_\odot$, in the radiation zone, energy is transferred from the core by thermal radiation, while convection is not present. Temperature drops from approximately 7 MK to 2 MK and density drops from 20 g/cm^3 to 0.2 g/cm^3. A transition layer, the tachocline, separates the radiative zone and the convective zone. In this region, the convection flows from the upper region slowly disappear to match the uniform rotation of the region underneath. here the magnetic dynamo seems to be created. In the Sun's outer layer, the convection zone, temperature and densities are lower, allowing convection to surpass radiation as energy transfer mechanism. At the photosphere, the temperature has dropped to 5700 K and the density to only 0.2 g/m^3. The photosphere is the layer below which the Sun becomes opaque to visible light. It is tens to hundreds of kilometers thick, it is not fully ionized and it is transparent to visible light. For this reason the spectrum emitted from the Sun is that of a black body at 5700 K. The photosphere has a particle density of $\sim$1023 m^{-3} (0.37% of the particle number at 1 atm). 500 km above the photosphere, there is a temperature minimum of about 4100 K. In the outer layers of the atmosphere, chromosphere, transition region, and corona, temperatures increases to much higher values than the surface of the Sun. The chromosphere is about 2000 km thick and presents a spectrum of emission and absorption lines that makes it visible during total eclipses. Temperatures in this region increase till 20000 K at top. The transition region is a thin layer in constant chaotic motion, where helium atoms are fully ionized and temperatures increase rapidly to coronal values of 1 MK. The corona is the extended atmosphere of the Sun, with a volume much larger than that of the solar disk and temperatures ranging from 1-2 MK to 20 MK. Flows of plasma from this region form the solar wind, that expands outwards forming the heliosphere, the tenuous outermost atmosphere of the Sun. The heliosphere begin approximately at 0.1 AU and envelops all the solar system in a spiral shaped magnetic field, until it impacts the heliopause more than 50 AU from the Sun.[39]

Thanks to the combined effort of the missions launched in the last 25 years, Ulysses, SOHO, TRACE, RHESSI, Hinode, STEREO and SDO, our knowledge of the Sun and its extended atmosphere has improved greatly. The outer layers and the solar wind have been studied and described, their capital importance due to the fact that the solar wind they create is responsible for many of the phenomena in Earth's magnetosphere and it seems to have influenced Mars and Venus evolution eroding their upper atmosphere. The characteristics of this flow of energy and matter, that expands outward from the corona, are well described. There are two types of solar wind, fast and slow. The former, moving at $\sim$700 km/s, arise from coronal holes,

areas of the Sun's corona where density of plasma and energy is lower, resulting in a darker and colder areas. The latter has a speed of ∼400-500 km/s and is formed in the equatorial region and around coronal holes, with a mechanism not yet clear. Fast wind has a rather steady flow, slow wind is more variable in speed, composition, charge state. At solar maximum the solar wind is a mixture of the two at all latitudes. Despite all the research and the descriptions of the solar environment in our possess, we do not yet understand the basic physical processes that heat the corona to millions degrees and accelerate the solar wind. Some experimental facts are not yet accounted for, for example, the fact that fast wind is originated in the coldest areas of the corona, and vice versa, appears strange. Different models have been developed to describe observations but data are insufficient to choose between them.

Instabilities and turbulence that fill the solar wind are another interesting aspects. Their dynamics differ from slow to fast wind and little is known about the forces that drive their evolutions, but is clear that dissipation of energy in a turbulent cascade contributes to the heating of the solar wind plasma.

Accompanying this continuous flux, are transient events, like flares, eruptive prominences, shock waves. The largest of these phenomena are the coronal mass ejections (CMEs), structures of magnetic field and material ejected from the corona at speeds up to 3000 km/s. This events are consequences of a build up of energy in areas where opposite magnetic fields are brought together and are the dominant way for the star to shed magnetic flux and helicity. These areas are called filament channels and are also source of the solar prominences, extensions of cold plasma, often with looped form, from the photosphere into the corona. Eruptions develop in 10-15', reaching in that brief time high energies ($\sim 10^{25}$ J). Traveling through the solar system they take the name of interplanetary CMEs (ICMEs), evolving from the original structure and causing interplanetary shocks and magnetic storms. Their trajectories are well studied, but there still is some uncertainty regarding source and initiation of the eruption, early evolution and also about their modification during heliospheric expansion. Solar wind and CMEs transport magnetic flux in the heliosphere, the former as open flux carried by fast wind from polar coronal holes, the latter as closed flux propagating with them. The total amount of magnetic flux changes over the solar cycle and also according with longer term variations. Correlation of flux variations with solar wind and CME's activity is still an unresolved issue.

Transient events act as particle accelerators, producing highly energetic particles that expand in the solar system as ionizing radiation. CME driven shocks can, on time scales of minutes, convert up to 10% of their kinetic energy in the production of relativistic energetic particles (SEPs). Shock waves form in the corona when CMEs or flares reach areas of slow moving plasma, usually in the lower corona for flares, or even at longer distances for CMEs. Shocks' turbulent magnetic field can impart

many small boosts to particles' speed, making them reach speeds near to that of light. Heated coronal loops and regions with reconnecting magnetic fields can also impart the same effect. Energy can also be transferred to particles on a single boost when magnetic loops rearranges explosively or reconnect, forming electric field that directly accelerate the particles. Independently from the accelerating cause, particles that undergo these processes possess enough energy to penetrate the ionosphere and reach ground level on Earth, affecting space hardware and disrupting communications. For this reason they are of great interest in the solar weather business. An interesting aspect of these particles is their arrival on Earth hours later than expected based on their velocity. This can depend on the fact that shocks needs several boosts to accelerate them, delaying their acceleration for many hours, or that shock's turbulence can trap the particles in scattered trajectory. It is at the moment not possible to understand the relative importance of the two phenomena. The low energy ions that form SEPs have the typical ionization states of the corona, showing that particles are accelerated in this region and not, for example, in flares loop. But this seed population seems to have suprathermal energies, with velocities from a few to a few tens of the solar wind speed. Origin and evolution of this population is still unknown.

The cause of all these phenomena is Sun's magnetic field, that moves plasma in the corona, drives its dynamics and produces the energetic events. Its activity follows a quasi-periodic 11-year activity cycle, a characteristic typical of many stars. The dynamo that generates the field is located in the convection zone. Meridional circulations and other near surfaces flows bring matter from decaying active region near the equator towards the poles, where subduction bring matters in the Sun interior, in the layer between convection zone and radiative zone (the tachocline). There, an opposite flow to the equator forms a 'conveyor belt' movement. Observations from past missions have studied rotations and meridional flows near the surface and at low latitude, but could not explore the high latitude regions. Near polar fields, rotation at high latitudes, meridional flow above 50° latitude and the return flow are not known. Polar field is directly related to the dynamo process and influences formation and evolution of many phenomena, polar plumes, X-ray jets, and polar coronal holes, that are the main source of the open magnetic flux that extends in the heliosphere. Understanding and describing these areas is then the only way to predict the behavior of solar wind and link it to the solar dynamo. Some simulations indicates that a local turbulent dynamo could be acting in the convection zone, contributing to the total magnetic flux. The effective presence of this process and its actual effects are still uncertain.

3.2 Scientific objectives of SolO

As highlighted in the previous section, there still are many unanswered questions about Sun, heliosphere and their dynamics. SolO seeks to answer these questions thanks to three important improvements it provides with respect to past missions. First is the close distance from the Sun, while at 1 AU interactions between plasma particles in the solar wind have already modified the initial structures present in the flow, at closer distances it will be possible to observe phenomena in the pristine shape they have when they are create in the corona, making it easier to link them to the dynamics that generated them on the Sun. The shape of the orbit will also provide a period of corotation of the spacecraft with the Sun near the perihelion, providing sight of a certain area of the surface for a longer period than possible from Earth, increasing detail and number of measurement. Second is the presence of the spacecraft of instruments that provide in-situ measurements along with instruments that will give remote measurement. In this way it will possible to monitor simultaneously solar surface, corona and heliosphere, following causes, birth and evolution of solar wind and transient phenomena. The last vantage point of the mission will be the adoption of a tilted orbit, that will reach at the end of the mission an inclination of 34° from the ecliptic, making it possible to observe accurately the polar regions.

SolO will address the central question of heliophysics: *How does the Sun create and control the heliosphere?*, answering physical problems that can be summarized in 4 main questions:

- How and where do the solar wind plasma and magnetic field originate in the corona?
- How do solar transients drive heliospheric variability?
- How do solar eruptions produce energetic particle radiation that fills the heliosphere?
- How does the solar dynamo work and drive connections between the Sun and the heliosphere?

Each one of these questions comprehend different aspects that the mission will evaluate and solve. In the following, a more accurate description of SolO's activities and targets is portrayed. The 4 questions will be broken up in three sub-questions and the ways SolO will adopt to solve them will be explained.

How and where do the solar wind plasma and magnetic field originate in the corona?

To address this question the first point to investigate is: *What are the source regions of the solar wind and the heliospheric magnetic field?* SolO will answer this question

measuring plasma and magnetic field in-situ and simultaneously performing remote sensing of photosphere and corona, to correlate wind to the source. Plasma parameters and compositional signatures of the wind will be related to spectroscopic signatures of coronal ions. Measuring energetic electrons, X-rays and radio emission and magnetic field in-situ and on the photosphere will allow tracing of magnetic field lines and reconstruction of the coronal magnetic field. EUV imaging and spectroscopy will give information on plasma state in the coronal loops, to understand dynamics of the transition region that can deliver material to the outer layers and monitor their evolutions.

The second focus of SolO will be: *What mechanisms heat and accelerate the solar wind?* Thanks to its high resolution in measuring the photospheric magnetic field and its imaging capabilities, SolO will identify plasma process such as reconnection and wave dissipation that are responsible for heating and acceleration. EUV imaging and spectroscopy will reveal energy variations and wave propagation tracing them to the source site. The heliospheric imager will measure velocity, acceleration, density of the structures traveling in the heliosphere. Comparison between data and existing models of acceleration profiles driven by turbulence and reconnection will allow us to verify model's predictions.

Then the question: *What are the sources of turbulence in the solar wind and how does it evolve?* will be addressed with electric and magnetic field measurement, along with distribution functions of protons and electrons determination, at many spacial and temporal scales. Measuring turbulences at various latitudes and distances, before stream-stream interactions can affect it, will provide determination of their evolution. High resolution will allow determination of small scale structures.

How do solar transients drive heliospheric variability?

The study of energetic events starts with the question: *How do CMEs evolve through the corona and inner heliosphere?* Observation with magnetograph, imaging spectrograph, soft X-ray imager, at close perihelion and in near-corotation with the Sun will provide a detailed description of ICMEs structures and relations with CME and mechanisms of conversion of magnetic into kinetic energy. The imaging spectrograph will observe CMEs in the inner corona, determining composition, expansion, rotation and energy distribution. Combining this information with in-situ measurements of plasma composition in ICMEs all the path of the evolving phenomena will be followed. Also a description of the magnetic characteristics of the structures and their role in accelerating particles will be useful to predict their effect on Earth.

Than the question to be addressed will be: *How do CMEs contribute to the solar magnetic flux and helicity balance?* SolO will measure the flux content of CMEs events directly and compare it with that of their source, linking flux content to the eruption process and quantifying the interplanetary dynamics on it. Measuring

suprathermal electron and energetic particles the spacecraft will diagnose the magnetic connectivity. Trajectories of these particles are in fact dependent on shape and connection of field lines, but are disturbed by scattering. For this reason a distance of only 0.28 AU is necessary to obtain good information. The flux contribution of small scale plasmoid, ejected by streamers, is not clear and will be investigated. Helicity content will be measured on the surface and in-situ, determining temporal evolution and changes before and after CME's launch.

Regarding the question: *How and where do shocks form in the corona and inner heliosphere?* SolO will need to acquire maps of the spatial distribution and temporal variations of plasma parameters throughout the corona. Polarized visible light images will provide maps of electron density and imaging of hydrogen and helium ions will help improve available plasma models. The spacecraft can locate and describe shock drivers (flares, CMEs) in the lower corona with a resolution of a few hundred kilometers and track their expansion in the region where shocks forms (2-10 $R_{\odot}$). In-situ measurement will characterize plasma and magnetic fields associated with the events, describing densities, turbulence, electric and magnetic fields.

How do solar eruptions produce energetic particle radiation that fills the heliosphere?

The first question: *How and where are energetic particles accelerated at the Sun?* requires a precise determination of the sequence of events that produce the acceleration and of the plasma properties of the suprathermal ions pool in the inner heliosphere. Almost every instrument on board will contribute to this task. Visible, UV, X-ray imaging will provide location and timing of flares loop and CMEs. X-ray will reveal interactions of particles at the loop footpoints. Radio waves will correspond to coronal shocks and escaping electrons. Magnetic fields and plasma measurements will identify and describe shock passages and their composition. Particle detection will identify SEPs themselves. Coronagraph will identify shock front speed, location and compression ratios during the rapidly evolution of the phenomenon. The arrival time in situ will be then linked to CME's position and speed, strength, turbulence, electric and magnetic fluctuation will be measured as the shock passes the spacecraft. This will provide a complete description of the acceleration process. The position close to the Sun will also allow observation of small phenomena, 15-20 times smaller than before, like X-ray originated from microflares, a possible candidate for coronal heating never studied from 1AU.

To be determined is also: *How are energetic particles released from their sources and distributed in space and time?* SolO will observe shocks evolving and will determine if acceleration is still taking place while they pass the spacecraft. It will determine if the time of arrival for enrgetic particles is due to the number of successive boosts they have to receive or if it is due to trapping. To do so it will confront

the delay time of particles with different energy and it will measure the turbulence, providing a complete model for the process. For SEPs emitted by loops or reconnection regions, UV and X-rays emissions will determine source location, radio emission o frelease electrons will allow tracing of paths and determination of magnetic field lines. During the corotational phase of the orbit, the spacecraft will scan active area for days acquiring a great number of field lines from its origins to the corona.

To understand *What are the seed population for energetic particles?* spectroscopic and in-situ measurements will describe the ion population. Variations between different shock events are expected and will be examined. The high latitude phase of the mission will have an important role, adding a third dimension to the map.

How does the solar dynamo work and drive connections between the Sun and the heliosphere?

Of particular importance to address this question is the adoption of a tilted orbit, because mapping of the magnetic flows has never been done at high solar latitudes. The capability of SolO in producing detailed maps even for the polar regions will be the crucial step forward with respect to past missions.

How is the magnetic flux transported to and reprocessed at high solar latitudes? The mission will measure local and convective flows, rotation, meridional circulation at different depth, revealing patterns, geometry, structures, properties of convection cells. It will be necessary to track small features even around the poles, acquire images of Doppler shifts, make use of helioseismic observations. Temporal variations will account for variations in the flow and tracking algorithms will be used to improve dynamic's predictions that at this time are inconclusive. Doppler maps of line of sight velocity will also reveal convection, rotation and meridional circulation flows. Thanks to helioseismology flows will be inferred through the convection zone to the tachocline and for the first time the analysis will be stereoscopic.

The second step will be to verify *What are the properties of the magnetic field at high solar latitudes?* The instrument will use its imaging instruments to characterize magnetic fields, plasma flows and temperatures of the polar regions, measuring for the first time polar megnetic flux and studying its transport from the activity belts towards the poles. It will probe the cancellation process that arise when flux elements of opposite polarity meet in the polarity reversal process. Along with other spacecrafts in the ecliptic it will determine the transversal magnetic field and allow a tridimensional view of the structures in the inner heliosphere. Adding imaging at visible and EUV wavelengths, it will study the effects of the magnetic field on the elements of the corona, like coronal holes and their boundaries.

The last point that will be addressed is: *Are there separate dynamo processes acting in the Sun?* To determine that it is necessary to study the distribution of

magnetic flux at different latitudes. A global dynamo will produce large magnetic features between 5° and 30°, and smaller activity at higher latitudes. A local turbulent dynamo will instead provoke a more uniform field. Once again, SolO's position outside the ecliptic will allow these measurement.

3.3 Payload

To fulfill the ambitious scientific objectives of the mission, an ensemble of 10 instruments was accurately selected. Their development is been carried on by ESA, NASA and ESA member states. It consists on a set of 6 remote sensing instruments and 4 for in-situ measurements, with a total mass of 180 kg and 180 W of power.

3.3.1 In-situ instruments

Energetic Particle Detector (EPD)

EPD will measure the composition, timing and distribution functions of suprathermal and energetic particles. Scientific topics to be addressed include the sources, acceleration mechanisms, and transport processes of these particles. The countries involved in its development are Spain, Germany, USA, ESA.

Magnetometer (MAG)

The magnetometer will provide in-situ measurements of the heliospheric magnetic field with high precision. This will facilitate detailed studies into the way the Sun's magnetic field links into space and evolves over the solar cycle; how particles are accelerated and propagate around the Solar System, including to the Earth; how the corona and solar wind are heated and accelerated. Developed in United Kingdom.

Radio and Plasma Waves (RPW)

The RPW experiment is unique amongst the Solar Orbiter instruments in that it makes both in-situ and remote-sensing measurements. RPW will measure magnetic and electric fields at high time resolution using a number of sensors/antennas, to determine the characteristics of electromagnetic and electrostatic waves in the solar wind. Developed in France, Sweden, Czech Republic, Austria.

Solar Wind Plasma Analyser (SWA)

SWA consists of a suite of sensors that will measure the ion and electron bulk properties (including, density, velocity, and temperature) of the solar wind, thereby

characterizing the solar wind between 0.28 and 1.4 AU from the Sun. In addition to determining the bulk properties of the wind, SWA will provide measurements of solar wind ion composition for key elements (e.g. the C, N, O group and Fe, Si or Mg). Developed by United Kingdom, Italy, France, USA.

3.3.2 Remote sensing instruments

Extreme Ultraviolet Imager (EUI)

EUI will provide image sequences of the solar atmospheric layers above the photosphere, thereby providing an indispensable link between the solar surface and outer corona that ultimately shapes the characteristics of the interplanetary medium. EUI will also provide the first-ever UV images of the Sun from an out-of-ecliptic viewpoint (up to 34° of solar latitude during the extended mission phase). Developed by Belgium, United Kingdom, France, Germany, Switzerland.

Multi Element Telescope for Imaging and Spectroscopy (METIS)

METIS will simultaneously image the visible and ultraviolet emission of the solar corona and diagnose, with unprecedented temporal coverage and spatial resolution, the structure and dynamics of the full corona in the range from 1.4 to 3.0 (from 1.7 to 4.1) solar radii from Sun center, at minimum (maximum) perihelion during the nominal mission. This is a region that is crucial in linking the solar atmospheric phenomena to their evolution in the inner heliosphere. Developed by Italy, Germany, Czech Republic.

Polarimetric and Helioseismic Imager

PHI will provide high-resolution and full-disc measurements of the photospheric vector magnetic field and line-of-sight (LOS) velocity as well as the continuum intensity in the visible wavelength range. The LOS velocity maps will have the accuracy and stability to allow detailed helioseismic investigations of the solar interior, in particular of the solar convection zone. Developed by Germany, Spain, France.

Heliospheric Imager (SoloHI)

This instrument will image both the quasi-steady flow and transient disturbances in the solar wind over a wide field of view by observing visible sunlight scattered by solar wind electrons. It will provide unique measurements to pinpoint coronal mass ejections (CMEs). Developed by USA.

Spectral Imaging of the Coronal Environment (SPICE)

This instrument will perform extreme ultraviolet imaging spectroscopy to remotely characterize plasma properties of the Sun's on-disc corona. This will enable matching in-situ composition signatures of solar wind streams to their source regions on the Sun's surface. Developed by United Kingdom, Germany, France, Switzerland, USA.

X-ray Spectrometer/Telescope (STIX)

STIX provides imaging spectroscopy of solar thermal and non-thermal X-ray emission. STIX will provide quantitative information on the timing, location, intensity, and spectra of accelerated electrons as well as of high temperature thermal plasmas, mostly associated with flares and/or microflares. Developed by Switzerland, Poland, Germany, Czech Republic, France.

3.4 Mission Design

After 15 years of studies and planning, a detailed and mature design of the mission and its components is available. The requirements derived from the scientific objectives were determined and satisfied in terms of mission, spacecraft and payload needs.

3.4.1 Requirements

There are several conditions that need to be satisfied in order to obtain the objectives foreseen for the mission. These requirements apply to mission and spacecraft and are listed here:

The orbit shall have the following parameters:

- Minimum perihelion radius larger than 0.28 AU to maximize the reuse of BepiColombo technology;
- Perihelion radius within 0.30 AU in order to guarantee multiple observations close to the Sun;
- Inclination with respect to solar equator increasing to a minimum of 25° (with a goal of 35° in the extended operational phase).
- At minimum perihelion passage, the spacecraft shall maintain a relative angular motion with respect to the solar surface such that individual solar surface features can be tracked for periods approaching one solar rotation;

- The Solar Orbiter system lifetime shall be compatible with a launch delay of 19 months (launch window locked to the next Venus gravitational assist opportunity).

The spacecraft shall be a 3-axis stabilized spacecraft using conventional chemical propulsion for orbit manoeuvres and attitude control, it will:

- Be able to accommodate the payload described in 3.3 and supply energy and thermal stability.
- Allow complete operation to all the payload complements for at least 3 periods of 10 days for each orbit, with a maximum of two contiguous periods. These periods will be typicallly centered on maximum northern heliolatitude, maximum southern heliolatitude and perihelion passage. In-situ instruments will be operational throughout the whole orbit.
- The spacecraft shall support a data downlink of 150 kbps at a range of 1 AU with the Malargüe ground station.

3.4.2 Orbit and time line

The launch is planned for September 2018 with a NASA-provided Evolved Expendable Launch Vehicle (EELV) from Kennedy Space Centre (KSC), USA. The launcher is an Atlas V 401. The Ariane 5 launcher from Kourou is currently the European back-up launcher. The trajectory of Solar Orbiter is entirely ballistic so that deterministic Deep Space Maneuvers are not required. Statistical mid-course maneuvers will be necessary for trajectory corrections and navigation of the gravity-assist maneuvers.

Direct injection into the required operational orbit is beyond the performance of the available launch vehicles. To obtain the necessary velocity and to raise the solar inclination angle to the required value repeated gravity assist manoeuvres (GAM) at Venus and Earth are necessary. This solution (if the september launch window will be confermed) yields a reasonable transfer phase duration of 3.25 years, a maximum distance to the Sun of 1.384 AU and a minimum perihelion of 0.286 AU. The initial period of the operational orbit is selected to be resonant with the orbital period of Venus (224.7 days), so that a sequence of Venus GAMs will gradually increase the solar inclination angle of the operational orbit. The mission profile foresee the launch, in September 2018, with an escape velocity from the Earth of 3.66 km/s and declination of the escape velocity of -41.5°. About 5 months after launch, a Venus GAM launches the spacecraft in a trajectory towards the Earth. An Earth GAM 10 months later puts the spacecraft into an orbit such that another Earth GAM occurs 22 months later. 2 months after the last Earth swing-by the spacecraft

arrives at Venus with a hyperbolic velocity of 19.3 km/s. A sequence of resonances 1:1-1:1-4:3-3:2-3:2 is then performed at Venus during the science phase such that the solar inclination is gradually raised up to the final maximum value of 34°. The maximum solar latitude is reached 7.6 years after launch.

3.4.3 Spacecraft design

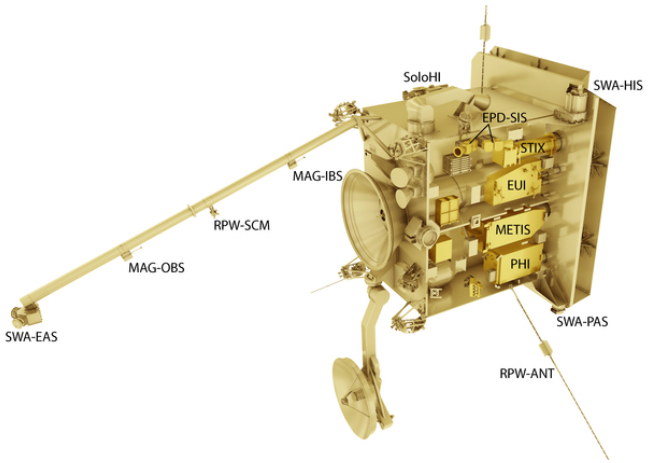

Figure 3.1. Graphic representation of SolO spacecraft, position of payload components is highlighted

The Solar Orbiter spacecraft (shown in fig. 3.1) is a Sun-pointed, 3-axis stabilised platform, 1800 kg in weight (of which 190 kg for the payload), 2.5×3×2.5 m, and with a power consumption of max 1100 W. A dedicated heat shield provides protection from the high levels of solar flux near perihelion. The spacecraft provides a stable platform to accommodate the payload in an electromagnetically clean environment. The 21 sensors were configured on the spacecraft to allow each to conduct its in situ or remote sensing experiments through 37 unobstructed fields-of-view. The spacecraft will also offer them protection from the solar environment. The remote-sensing instruments are located on a very stable platform with 2' co-alignment. Their 1"-over-10 s Relative Pointing Error performance and long science windows, will allow simultaneous and high-resolution observations. Solar Orbiter has inherited technology from previous missions. The solar arrays, for example, replicate those of the BepiColombo Mercury Planetary Orbiter. They can be rotated about their longitudinal axis to avoid overheating when close to the Sun. A battery pack provides supplementary power at critical periods such as eclipses encountered during planetary flybys. The communication link with the Earth takes place in X-band. The subsystem supports simultaneous telemetry, telecommand and ranging. Low-Gain Antennas (LGAs) are used for Launch and Early Orbit Phase (LEOP) and will

also be available as a back-up during the mission phase when steerable Medium- and High-Gain Antennas will be in use. The High-Temperature High-Gain Antenna needs to point to a wide range of positions to achieve a link with the ground station and to be able to downlink sufficient volumes of data. Its design was adapted from the BepiColombo mission. The antenna must also cope with a high thermal load. Due to the mission's unique orbit, the throughput of the data downlink is highly variable. Most data will therefore initially be stored in on-board memory and sent back to Earth at the earliest possible opportunity.

The space segment of the mission, comprised by spacecraft and payload, will be sustained by a launch segment, composed by the Atlas V rocket, which has enough launch capacity for the expected 1800 kg spacecraft separated mass plus the 1194 mm diameter adapter.

To complete the mission profile, the ground segment will maintain communications with the spacecraft. It is formed by Operations Ground Segment and Science Ground Segment. The former comprises three ground stations and the Mission Operations Centre (MOC). The MOC is located at the European Space Operations Centre (ESOC) in Darmstadt, Germany, and is responsible for performing all mission operations and raw data archiving and distribution to the instrument teams. The receiving ground stations are: Malargüe (nominal for all operations throughout the mission), New Norcia (back-up for all operations in critical phases where additional tracking support is required), Cebreros (back-up when Malargüe is down for maintenance, and back-up for all operations in critical phases where additional tracking support is required). The Science Ground segment consists in the Science Operations Centre (SOC), located at the European Space Astronomy Centre (ESAC) in Madrid, which will be responsible for mission planning and generation of payload operations request to the MOC as well as science data archiving.

3.5 METIS

Among the remote sensing instrumentation on board of the Solar Orbiter, the coronagraph METIS (Multi Element Telescope for Imaging and Spectroscopy) will acquire images of the solar corona between 1.6 and 3 $R_\odot$ (at perihelion). It will analyze visible light emission between 580 and 640 nm and its polarization, and hydrogen emission at Ly-α.[40]

3.5.1 Imaging of solar corona

METIS will perform its tasks of visible and UV imaging simultaneously. The level of detail will be unprecedented for temporal coverage and with a spatial resolution down to 2000 km. With these characteristics it will be able to describe structures

and dynamics of the corona inside its field-of-view (FOV) range from 1.5° to 2.9°. This corresponds to 1.6 to 3.0 $R_{\odot}$, at minimum perihelion (0.28 AU), and from 2.8 to 5.5 $R_{\odot}$, at 0.5 AU. METIS will obtain full coronal images with high temporal cadence (up to 1 s in visible-light, up to 5' in the UV), and plate scale (20 arcsec in the UV, and 10 arcsec in the visible).

METIS capabilities will help to absolve many of the scientific objective foreseen for SolO mission, absolving the following functions:

- Production of high quality images of the corona;
- Mapping of H flow velocities and velocity distributions and electrons density;
- Describing velocity and mass of evolving structures.

The instrument not only will photograph coronal evolution, but it will characterize hydrogen dynamics, giving information on its main physical parameters (i.e. density, temperature and outflow velocities), and also will observe temporal and spatial evolutions of features propagating in the corona. The information will be useful for:

- Analysis of composition of coronal source regions;
- Understanding of wave propagation and heating;
- Time history of velocity and brightness of solar wind features;
- Mapping CMEs source location, expansion, rotation, and composition through corona; comparison with properties measured in-situ;
- Determination of position, speed and timing of shock events;
- Imaging of loop, flares and CMEs (particularly its longitudinal extent);
- Imaging of coronal and heliospheric structure;
- Imaging of evolution of coronal hole boundaries;
- Determination of velocities and mass density of evolving structures;
- Mapping source regions to in-situ properties of magnetic connectivity, polarity, and helicity;
- Determination of timing of eruptions and coronal manifestations;
- Global mapping of electron densities and H flow velocities;
- Analysis of turbulence properties throughout the inner heliosphere and corona;
- Mapping of coronal suprathermal ion pool.

3.5.2 Instrument layout

METIS is an externally occulted Gregorian telescope. Fig 3.2 shows the optical elements of the instrument.

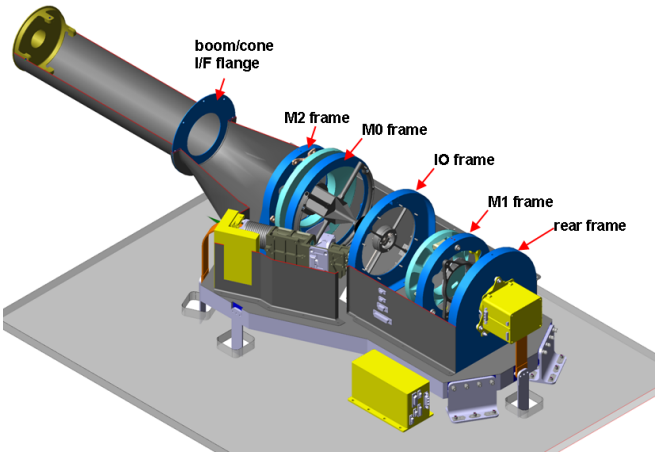

Figure 3.2. Design of METIS

The external occultation provides an aperture that highly vignettes the lower heliocentric heights, reducing the large dynamic range of the coronal signal. The occultation scheme is based on an inverted external-occulter (IEO). This original design reduces the thermal load in the instrument with respect to a classical design (by two order of magnitude on the rejection mirror). The on-axes design (shown in fig. 3.3), which substitutes the off-axes initial design, was adopted for the same reason.

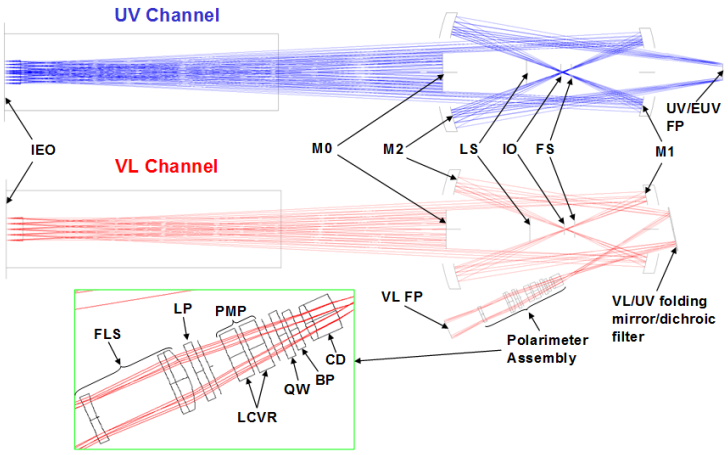

Figure 3.3. METIS VL and UV paths

The IEO is also the entrance pupil of the instrument and consists of a circular

aperture (ø 40 mm). It is located at the far end of a 800 mm boom located in front of the telescope.The disk-light through the IEO is rejected back by a spherical heat-rejection mirror (M0, ø 71 mm) up to 1.1° (i.e. 1.17 $R_\odot$ at 0.28 AU). The coronal light, on the other hand, is collected by the optics of the telescope. The primary ellipsoidal mirror M1 collects the corona-light and constructs the image in the focal plane of the secondary ellipsoidal mirror M2 which focuses the corona image in a second focal plane behind the primary. The suppression of the diffracted light off the edges of the IEO and M0 is achieved, respectively, with an internal occulter (IO) and a Lyot trap (LS). The VL and UV paths are split by an UV interference filter at 12° angle of inclination with respect to the optical axis. The MgF_2/Al coatings in the primary (M1) and secondary (M2) telescope mirrors are optimized for enhanced reflectivity at 121.6 nm. The coating has also high reflectivity in the visible-light. The UV narrow bandpass interference filter acts as VL-UV beam splitter by selecting the 121.6 nm UV band in transmission (with a FWHM of 10 nm) and reflecting the VL to the polarimeter. The visible light polarimeter is composed by a liquid crystal variable retarder together with a fixed half-wave retarder and a linear polarizer in "Sernamount" configuration. Inside the polarimeter a broad band filter selects the VL bandpass (580-640 nm). The UV and VL detectors are, respectively, an intensified active pixel sensor (IAPS) with scale factor 20 arcsec/pixel and image size of 30.7 mm (1024×1024) with 30 μm equivalent pixel size; and an APS with scale factor 10 arcsec/pixel and image size: 20.5 mm (2048×2048) with 10 μm equivalent pixel size. In the spacecraft is planned a door mechanism which closes the instrument aperture when METIS is not used.

The METIS instrument architecture consists on the following functional elements:

1. METIS Optical Unit (MOU), consisting of two separate physical units, functionally belonging to the MOU:
   - Optical Bench Unit (OBU), consisting of the optical bench and the mechanical supports, the optical train from the external occulter to the focal planes, the detector assemblies, the mechanisms for the instrument operation, the thermal control hardware.
   - The harness interconnecting all the METIS physical units.
2. METIS Processing and Power Unit (MPPU). The electronic unit which manages the instrument operations, acquires and processes the detectors data, controls the mechanisms and the thermal hardware installed on the MOU, and provides the power and data interfaces of METIS with the spacecraft.
3. METIS flight software, loaded in the MPPU and implementing the instrument operation and control functions.

The METIS Optical Bench Unit (OBU) is the core of the instrument, lodging all the optical elements (Opto-Mechanical Subsystem), the detectors (Detection Subsystem) and also the Thermal Control Subsystem (consisting in heaters, thermo-electric cooler, thermal straps, multi-layer insulator, ...)

The overall structure will have a mass of 19.20 kg and operate with 18.08 W of power. The 90×44×25 cm optical bench will fit on its spacecraft housing. Dimensions of the electronics are 22×25×10 cm. Table 3.1summarizes METIS performances.

Table 3.1. Performences of METIS

Parameter	Performances
Wavelength range	VL:580-640 nm UV: 121.6±10 nm
Effective focal length	VL: 200 mm UV: 300 mm
Spatial Plate scale	10 arcsec (VL) 20 arcsec (UV)
Field of view	1.5° - 2.9° annular, off-limb corona 1.6-3.0 $R_\odot$ @ 0.28 AU 2.8 - 5.5 $R_\odot$ @ 0.5 AU
Average Instrumental Stray Light ($B_{stray}/B_\odot$)	VL: $< 10^{-9}$ UV: $< 10^{-7}$
Temporal resolution	VL: 1-450 s UV: 1-30'
Broad-band Linear Polarization Sensitivity	$\leq 10^{-2}$
Signal-to-Noise Ratio	VL > 7 (7-590) UV > 3 (3-86)
Telemetry rate	10.5 kbit/s

Chapter 4

Optical elements for 121.6 nm on METIS

METIS will operate in a harsh environment, where the thermal load due to solar radiation will be tremendous. For this reason the amount of light entering the instrument will be reduced to a minimum thanks to appropriate choices in the architecture of the telescope. At the same time the target of the instrument is to detect the radiation originated from the corona, which is much fainter than the unwanted solar disk radiation.

To keep the intensity of the incoming radiation to an acceptable level, the efficiency of the optical elements must be the higher possible, especially for the UV path, which is the more critical. The interference filter will have for this reason a novel design, never tested in past missions, granting an efficiency higher than ever.

4.1 Materials

In the VUV the choices available for optical materials are limited, and since the 1950s the classical coupling of aluminum (Al) and magnesium fluoride (MgF_2) has not been surpassed. Table 4.1 shows the properties of the two materials.

Al is the material that gives the best reflectivity in the VUV. Its properties strongly depends on deposition conditions. The more deposition time increases, the more reflectivity decreases (increasing the deposition time from 2 to 55 s, reflectivity at 160 nm decreases from 73% to 64%, at a pressure of 10^{-5} mmHg); for optimum results deposition time should be of 1-2 s (a deposition rate > 30 nm/s is needed).[41] Degradation of performances with deposition time is more accentuated if pressure in the deposition chamber is higher (films deposited at a rate of 3 Å/s at $5 \cdot 10^{-9}$ mmHg have a reflectivity 30% higher than films deposited at $3 \cdot 10^{-6}$ mmHg).[42] Temperature of the substrate must be lower than 50℃, because along with temperature,

Table 4.1. Physical properties of Al and MgF_2

Physical property	Al	MgF_2
Molar mass (g/mol)	26.9815	62.3018
Melting point (K)	933.47	1536
Boiling point (K)	2743	2530
Density (g/cm^3)	2.70	3.148
Crystal structure	fcc	Rutile (tetragnal)
Refractive index @121.6 nm	0.042	1.63
Extincion coefficient @121.6 nm	1.14	0

crystal size and therefore surface roughness increase, limiting reflection, especially at shorter wavelengths.[43]

For wavelengths shorter than 160 nm, contribution of impurities, and particularly the presence of aluminum oxide (Al_2O_3) strongly influences the optical properties of the film. Al forms in fact a native oxide layer $\sim$2 nm thick that limits the reflectivity to values lower than 30%.[44] To maintain the pristine high reflectivity of Al above 80 nm (greater than 86% @121.6 nm), a protective coating is necessary. MgF_2 is transparent for wavelengths longer than 115 nm and its optical constants present a good coupling with those of Al, providing a good reflection at the interface. LiF is the only other material with adequate transparency characteristics at 121.6 nm (its cutoff wavelength is 105 nm), but its coupling with Al doesn't give results as god as those of MgF_2 and also tends to degrade under atmosphere condition. For these two reasons MgF_2 is prevalently used as Al capping layer.[45] MgF_2 is best deposited by evaporation on heated substrate (200-300°C), because deposition at room temperature produces a porous structure that easily absorbs water.[46]

4.2 Mirrors for Ly-α

The structure of a mirror reflecting in the VUV is composed by an Al layer that must be at least 70-80 nm thick, to essentially eliminate any VUV transmittance. On top is deposited a MgF_2 layer, whose thickness is optimized to increase reflection by constructive interference. At Ly-α this thickness is 25 nm.

Classically, preparation of this structure is carried on with evaporation techniques. The target material is evaporated by resistance heating or electron beam in experimental chambers under vacuum conditions ranging from 10^{-6} to 10^{-9} mbar. The necessity of high deposition rates to maintain Al purity and uniformity, makes evaporation more attractive than other techniques, such as sputtering, that cannot reach the same performances.

The MgF_2 layer deposited by evaporation also presents good stoichiometric and roughness characteristics, but grows in a porous structure with a packing density of only 0.7, causing extreme sensitivity to moisture in room air. The pores become filled with water when exposed to atmosphere, affecting the stability of their optical and mechanical properties and inducing undesired optical losses in the film.[46] Heating the substrate before deposition could solve this problem, producing a more densely packed structure, but these conditions are incompatible with the integrity of the Al layer underneath and they have not produced reflectivity improvements.[45]

Standard evaporated Al/MgF_2 mirrors have reflectance at 121.6 nm around 80% (eSource optics provide devices with efficiencies between 77-80% and Acton guaranties efficiency $> 80\%$). Data form literature give values of reflectivity around 82-83% for many authors.[44, 47, 48] The best obtained result is 85%, obtained by Bradford et al, that improved their previous results by 2% adopting a bigger deposition chamber with high heating capabilities and various devices to make deposition uniform.[49]

Recently, alternative techniques were suggested. Ion assisted deposition (IAD) and Ion-beam sputtering (IBS), are processes that allow formation of a more packed structure even at room temperature conditions. IAD acts bombarding the growing film with ions, that disrupt the porous structures and give to the atoms of the forming layer the energy to rearrange in a compact film. These process, though, present some inconveniences, the film it produces tend in fact to be non stoichiometric, with fluorine deficiencies that, filled by oxygen atoms, increase VUV absorptions. Even deposition in a reactive environment (with presence of F_2 gas) can only partially overcome the problem.[50]

IBS produces films with similar characteristics to those produced by IAD, with good packing and stability but bad stoichiometry. It presents the added difficulty of Al layers quality; in fact sputtering deposition rates are slower and oxygen incorporation decrease Al quality. Larruquert et al. produced good VUV mirrors with a combined technique that involved evaporation of the Al layer and IBS of MgF_2.To implement this system is necessary a facility that contains both evaporation sources and sputtering components. Even so, the obtained reflectivity did not exceed 85%.[48]

4.3 Interference filter

While the efficiency of standard Al/MgF_2 mirrors is well adequate for the purposes of METIS, the interferential filter, that will separate the optical path of visible and UV light and select a narrow band around 121.6nm, will have more stringent requirements[51]:

- Physical characteristics:

  - Substrate: MgF_2 crystal cut $\perp$ to optical axis
  - Clear Aperture (ø): 72.8 mm
  - Thickness: 6 mm
  - Wedge angle between surfaces: 0.148°
- It shall work at an incidence angle of 12° with respect to the optical axis;
- Surface flatness $\leq \lambda/10$ rms, $\lambda = 632$ nm;
- Interference coating performance:
  - Reflectance in VL$>$ 80% at 584 nm
  - Wavelength peak = 121.6 nm
  - Transmission peak at 122 nm $>$ 20%
  - Interference coating FWHM = 15 nm
- The central area of the interference filter with a diameter of 37 mm shall be coated with a coating opaque to UV.

The optical performances are at the limit of present technology and have never been used for space applications before. Previous missions in fact, could afford smaller efficiencies due to the easier environmental conditions in which they operated. Interferential filter that can achieve these results are multilayers working as Fabry-Perot interferometers. Fernandez-Perea et al. produced a 4 layer design ($Al/MgF_2/Al/MgF_2$) deposited on a MgF_2 substrate with 20.5% transmittance at 121.6 nm and FWHM of 12 nm. The facility used for the task is a UHV deposition chamber with capability for thermal deposition, sputtering and UV reflectometry.[52] Those results are the same obtainable by industrial facilities (Acton).

Chapter 5

Instrumental setup

The purpose of the three years of this PhD is related to METIS and its investigation of solar hydrogen emission. At the CNR-IFN laboratories in Padova (Italy) there are facilities that allow deposition of metals and dielectric materials and their optical and morphological characterization. Their performance had never been tested and the optimization of a process aimed to produce competitive optical elements in METIS working range was the focus of this work. I deposited Al and MgF_2 layers, individually at first and then combined, for the first time in those facilities. Different phases of this path involved testing the behavior of deposited materials varying the conditions in the experimental chamber, deposition and optimization of mirrors reflecting at Ly-α, measurement of their optical and structural properties, treating of the obtained samples with annealing techniques.

In this chapter I will describe the equipment that allowed the progression of this project, from deposition to characterization and post deposition treatment.

5.1 Deposition facilities

There are two deposition facilities available in the CNR laboratories. The first one is an RF magnetron sputtering (shown in fig. 5.1). Sputter deposition is a physical vapor deposition (PVD) method that involves ejecting material from a "target" that is a source onto a "substrate". A sputtering gas, usually an inert gas such as argon, is present in the chamber and it is heated into a plasma by electric fields. The ions present in the plasma are then accelerated towards the target, hitting its surface and causing emission of the sputtered atoms. 99% of the ejected atoms have no charge and can reach the substrate on ballistic trajectories without being affected by the fields present in the chamber. Controlling the gas pressure in the chamber, the number of collisions of the sputtered atoms can be varied, regulating their arrival energy on the substrate from high-energy ballistic impact to low-energy

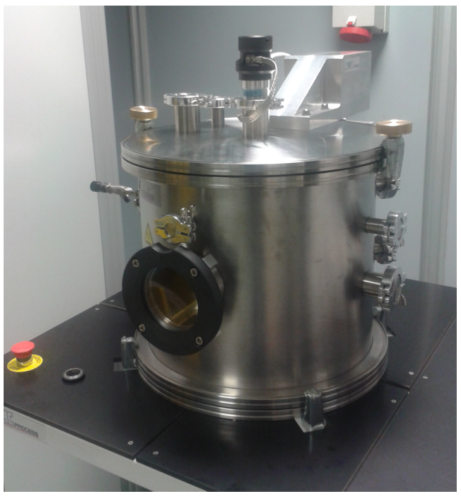

(a) External view of the sputtering deposition chamber

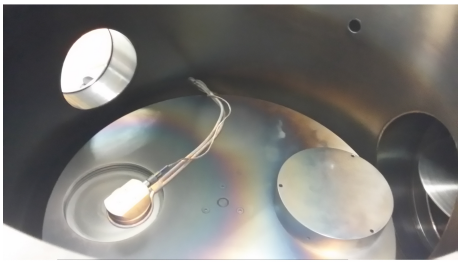

(b) Internal view of the sputtering deposition chamber. On the left, the golden microbalance is hovering on the Si target

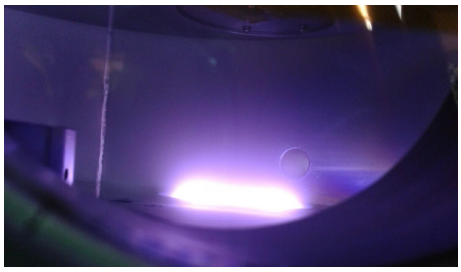

(c) Ar plasma heated inside the facility, confined by the magnetron on a toroidal region above the target

Figure 5.1. Photos of the RF magnetron sputtering facility.

thermalized motion. For efficient momentum transfer, the atomic weight of the sputtering gas should be close to the atomic weight of the target, so for sputtering light elements neon is preferable, while for heavy elements krypton or xenon are used. Reactive gases can also be used to sputter compounds. The compound can be formed on the target surface, in-flight or on the substrate depending on the process parameters. The availability of many parameters that control sputter deposition make it a complex process, but also allow experts a large degree of control over the growth and microstructure of the film. The low temperatures involved are also an advantage in certain cases.

In our facility the sign of the anode-cathode bias that generates the plasma is varied at radio frequency rate, to avoid charge build-up on insulating targets. A

magnetron utilizes strong electric and magnetic fields to confine charged plasma particles close to the surface of the sputter target. Electrons confined by magnetic fields on helical paths undergo more ionizing collisions with gaseous neutrals near the target surface than would otherwise occur. This effect allows for higher deposition rates and it also means that the plasma can be sustained at a lower pressure.

The facility at our disposal is equipped with two target holders of 4" ø, that can be operated alternatively producing multilayers of two different materials. An high voltage radio frequency (RF) generator, that produces 600 W impulses at 13.56 MHz, lights the plasma in the argon flow injected in the chamber, two substrate holders are suspended on a plate attached to the chamber lid facing the target. A magnetic field confines the plasma on a ring above the target. A mass flow controller set for oxygen and argon flows measurement allows for reactive sputtering. Levels of vacuum of 10^{-6} mbar are provided by a turbomolecular pump (Pfeiffer TC 400) and a cryogenic pump (Edwards coolstar 800). The facility is used for deposition of multilayer optics in the EUV. Because of the reasons described in subsection 4.2 this facility is not suitable for the Al depositions of this work and was not employed.

The materials treated in this work required deposition by evaporation. The evaporation involves two basic steps: a hot source material evaporates and then condenses on the substrate. Its a process that requires high vacuum, so that evaporated particles can travel directly to the deposition target without colliding with the background gas. At a typical pressure of 10^{-6} mbar, a 0.4-nm particle has a mean free path of 60 m. During deposition, though, hot objects in the evaporation chamber, such as heating filaments, produce unwanted vapors that limit the quality of the vacuum. Collision with foreign particles may cause unwanted reaction (an example related to this work regards aluminum, that, if deposited in the presence of oxygen, will form aluminum oxide). They also reduce the amount of vapor that reaches the substrate, which makes the thickness difficult to control. Because the evaporated material attacks the substrate mostly from a single direction, protruding features block the evaporated material from some areas. This phenomenon is called "shadowing" or "step coverage".

Evaporation systems include a deposition chamber, a vacuum system and an energy source that evaporates the material to be deposited. Many different energy sources exist:

Thermal method Materials (in the form of wire, pellets, shot) are placed onto heated semimetal (ceramic) evaporators known as "boats". A pool of melted metal forms in the boat cavity and evaporates into a cloud above the source. Alternatively the source material is placed in a crucible, which is radiatively heated by an electric filament, or the source material may be hung from the filament itself (filament evaporation).

Electron-beam The source is heated by an electron beam with an energy up to

(a) External view of the e-beam evaporation chamber

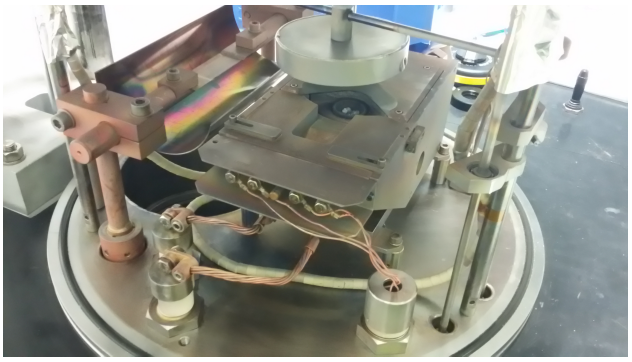

(b) View of the evaporator internal constituents

Figure 5.2. Photos of the e-beam evaporation facility.

15 keV, produced by a current passing through a filament (usually tungsten) thanks to thermionic emission, and directed on the crucible containing the target with magnetic fields.

Flash evaporation A fine wire of source material is fed continuously onto a hot ceramic bar, and evaporates on contact.

Resistive evaporation Is accomplished by passing a large current through a resistive wire or foil containing the material to be deposited.

With respect to sputtering, deposition rates obtainable by evaporation are higher but with higher shadowing effect. There is no risk of damaging the growing layer by sputtering from gas ions, there are less parameters that can be used to influence the microstructures of the growing films. All this aspects can be an advantage or disadvantage, depending on the desired result.

The facility adopted in our laboratory is an e-beam evaporator produced by IonVac Process srl (fig. 5.2). The vacuum chamber is a cylinder 52 cm high and with a 35 cm diameter. A Varian Turbo-V 550 turbomolecular pump in series with a scroll pump provides a base vacuum of $\sim 10^{-7}$ mbar. A Temescal systems apparatus generates the electron beam; the main supply CV-6SL generates currents up to 30 A, that heat a tungsten filament, causing emission of the e-beam with currents of hundreds of mA. The direction of the beam is controlled by magnets and a sweeper directs it on the target material, enabling motion of the beam in the

longitudinal and latitudinal direction at various amplitudes and frequencies. The chamber can contain up to 4 different target materials, positioned in crucibles of 1.167" ø and 0,563" h. Target materials are provided by Kurt J. Lesker Company and are Al pellets 1/8"ø×1/8"length of purity 99.999% and MgF_2 pieces of purity 99.9%. Intensity of the beam can be tuned to provide the desired heating of the target and consequently the desired evaporation and deposition rates. The evaporated materials deposit on substrates hanging from the top of the chamber that can be rotated to improve uniformity of the final layer. Heating of the substrate is performed with three quartz lamps (64576 OSRAM 1000 W 230 V base G×6.35); the system can reach temperatures of 300-400℃ and a thermocouple allow temperature control. An Inficon quartz microbalance monitors growth of the forming layer with nanometric precision.

5.2 Optical characterization facilities

For the analysis of the optical performances the lab offers several solutions, allowing measurements of transmittance and reflectivity from soft X-rays to IR.

A Varian Cary 5000 high performance UV-Vis-NIR spectrophotometer covers the range from 200 nm to 3300 nm (fig. 5.3. The instrument adopts a mercury lamp for the UV range and a visible lamp for the remaining parts of the spectrum. The setup provides various configurations, that can test transmittance, specular reflectance at varying angles and diffuse reflection, of solids, liquids and gases. Figure 5.4 shows a scheme of the instrument.

Two homemade facilities cover the higher energy part of the spectrum. The first is a setup that operates with a hollow cathode lamp or a Manson X-ray source

Figure 5.3. Spectrophotometer Cary 5000

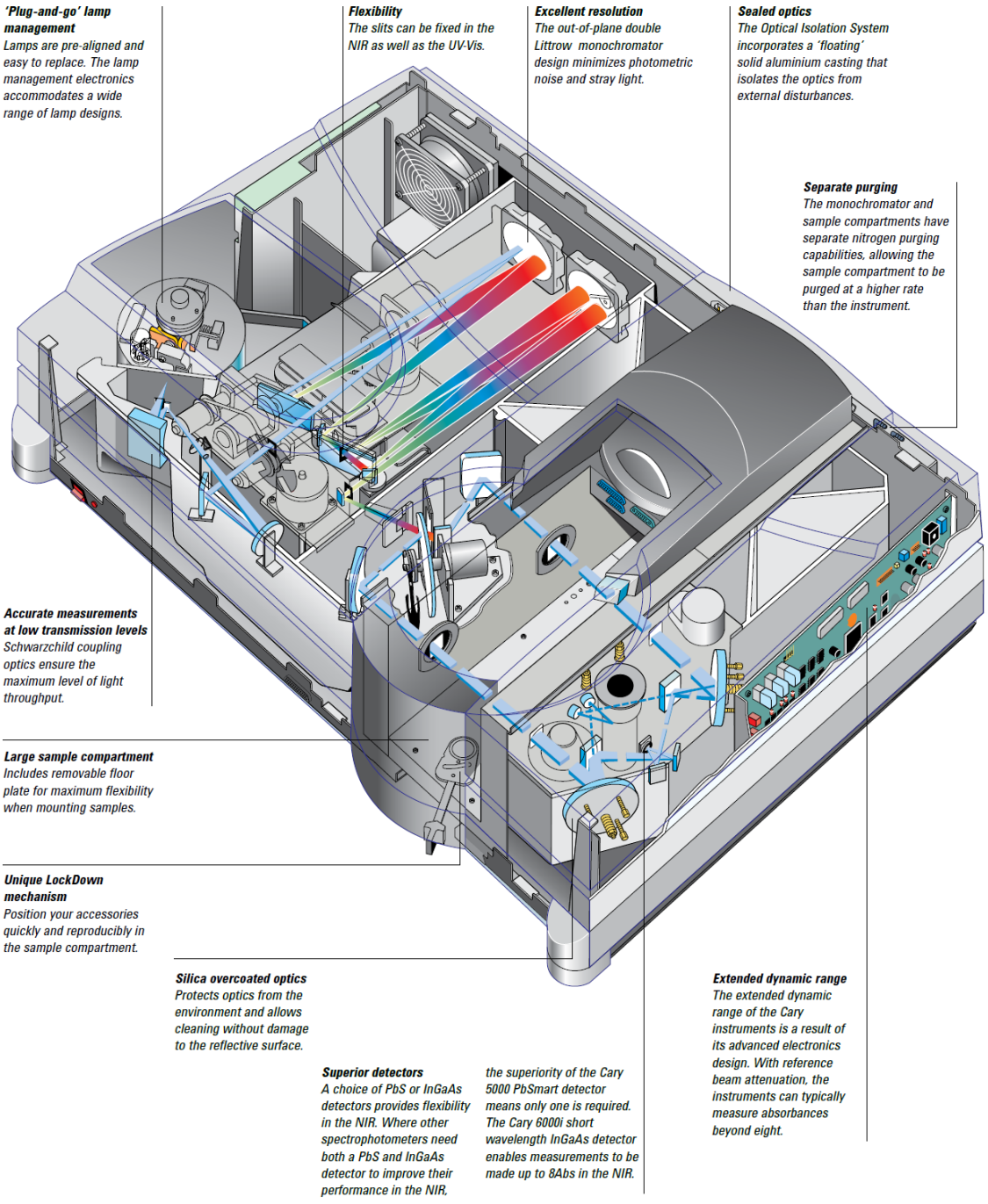

Figure 5.4. Spectrophotometer Cary 5000 operational scheme and structure

and a series of optical elements working at grazing incidence. A pumping system provides the high vacuum level necessary to avoid absorptions from air and the setup is optimized to work with radiation at wavelengths ranging from a few nanometers to ∼30 nm.

(a) Photo of the facility setup

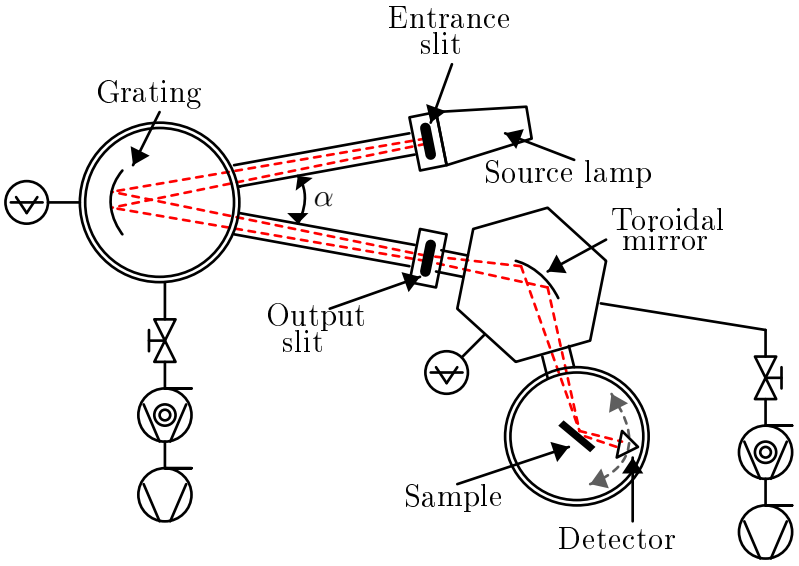

(b) Optical layout of the facility

Figure 5.5. Normal incidence facility.

The last facility, a normal incidence reflectometer, performs spectroscopic analysis from 30 nm to 300 nm, covering the range of interest for the materials of this work. It is formed by three connected vacuum chambers, operating at a vacuum of 10^{-6} mbar thanks to two turbomolecular pumps. The first, connected to the

first chamber, is a Leybold Turbotronic NT-360 V. The second, connected to second chamber, is a Varian Turbo-V 300. Fig. 5.5 shows a photo and the structure of the facility. The first chamber hosts a toroidal grating, working as a monochromator mounted in Johnson-Onaka configuration. A Cinel step motor rotates the monochromator to select the operative wavelength. The second, hexagonal chamber, presents a toroidal mirror, which focuses the beam at the center of the third chamber, where the samples are positioned. Two vertical slits, mounted respectively in front of the lamp and in the focus position between grating and mirror, regulate spectral resolution and dimensions of the spot.

Different sources are compatible with the facility. A homemade hollow cathode lamp (shown in fig. 5.6 produces different line spectra in the EUV, at discrete wavelengths depending on the fluxed gas (Ar, Ne, He, N). A Hamamatsu D2X2 deuterium lamp produces a continuum from 115 to 400 nm, whit a peak at 121.6 nm (the spectrum shown in fig. 1.2). At wavelength longer than 200 nm the facility can operate at atmospheric pressure, with a mercury lamp that emits a continuum around the 253.7 nm peak. The detector is mounted on a rotating support, that can revolve around the sample in a $\theta/2\theta$ configuration. It collects light in transmission and at different angle of reflection, from 10° of incidence to grazing incidence. For the EUV and VUV region the detector is a CEM, solar blind and operating only at pressures below 10^{-4} mbar. At longer wavelengths a photomultiplier tube absolves the function.

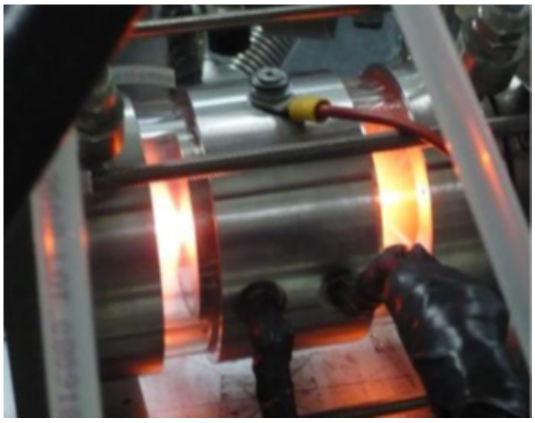

Figure 5.6. Hollow cathode lamp.

Whenever necessity for more accurate measurements called, they were carried on at BEAR (Bending magnet for Emission, Absorption and Reflectivity beamline), at the Elettra synchrotron facility in Basovizza (TS), Italy. The synchrotron is formed by a linear accelerator and a booster that accelerate electrons to energies of 2 GeV, and a storage ring that keeps them on a circular trajectory, thanks to electric

and magnetic fields synchronized with the electron bunches. The particles, accelerated radially by bending magnets and insertion devices (undulators and wigglers) while traveling at relativistic speeds, emit radiation with unique characteristics: relativistic Doppler effect and length contraction move the frequency toward X-rays, providing to the users a broad spectrum of light, polarized linearly on the ring plane and circularly outside the plane. Important emission characteristics are high flux, brilliance, collimation and stability. The unmatchable intensity of synchrotron radiation allowed for more precise determination of the optical characteristics of our samples. BEAR offers an UHV environment that operates in the 5-1600 eV spectral region (roughly corresponding to the range 1-250 nm), delivering elliptically polarized radiation with the possibility of ellipticity selection from linear to near circular polarization, with an energy resolution ≥ 3000 over the whole energy range and final spot size of the order of 10×100 μm^2; all with an appreciable flux. Three different monochromators and several optical filters guarantee monochromaticity throughout the energy range. The available spectroscopic tools of the facility include Specular and diffuse reflectivity, XAS, Fluorescence yield, Luminescence yield, XPS-UPS, TEY, photoelectron diffraction.[53]

5.3 Surface analysis facilities

A simple way to gain an understanding on the quality of the deposition is to implement a physical scan of the surface and collect information about roughness, and consequently microstructure and growth dynamics.

Figure 5.7. XE-70 atomic force microscope.

The task is well addressed by the Park Systems XE-70 atomic force microscope

(fig. 5.7. Atomic-force microscopy (AFM) is a very high-resolution type of scanning probe microscopy (SPM), a branch of microscopy that forms images of surfaces using a physical probe that scans the specimen. An image of the surface is obtained by mechanically moving the tip of the probe in a raster scan of the specimen, line by line, and recording the probe-surface interaction as a function of position, reconstructing the 3D topography of the sample.

AFM calculates the distance probe-sample by measuring the force between them, which can be a Van der Waals attraction (non contact mode) or Coulomb repulsion (contact mode). In both cases the interaction is function of the distance; in contact mode repulsive forces present sharp variations, providing a better resolution of the instruments, higher scan speeds, easier scans in samples with high roughness. But, being the tip nearer to the sample, lateral forces can distort the images and produce damages in soft samples.

In non contact mode forces and gradients involved are very low; to improve the system sensitivity and the signal/noise ratio a lock-in technique is needed: the cantilever (the beam on which the tip is attached) is forced into vibration at its resonant frequency. Changes in the force gradient entail a modification of the resonance frequency, reducing the oscillation amplitude. This modification in the oscillation is translated into an electric signal and converted in topographical information. Usually the signal is used also as feedback, in order to keep constant the tip-sample distance, but scan can be also made at constant tip height. An alternative way to work is the "semicontact mode" in which the tip oscillates between the two zones.

XE-70 can work in all the three modes and it is also equipped with an external module for operation in current mode, which applies a bias between tip and sample, registering current flow variations. This is not used to produce topographical images but to give information about material's conductivity or to induce oxidation in selected areas of the sample. Other alternative AFM uses involves lateral force microscopy, which give information on consistency and friction of surfaces, lithography and atomic manipulation.

During this work, the instument was mainly used in non contact mode, with the tip scanning small portions of the samples and registering variations of the van der Waals forces between tip and surface as the latter approaches or separates from the tip, according to its morphology. The tip, a PPP-NCHR non contact cantilever with a radius of less than 10 nm, could obtain tridimensional images with vertical resolution of a few Ångström and lateral resolution limited only by the number of pixels of the image. Scanned areas range from less than 1×1 μm to areas of 100×100 μm. Piezoelectric scanners ensure maximum accuracy of tip and sample movements, along the z axis for the tip and along the x,y plane for the sample. An optical microscope helps for a rough alignment of the sample under the tip. To transform the oscillation of the cantilever in a measurable electric signal, a laser diode is used, which is first reflected by the cantilever, than detected by a split

photodiode. Insulation from ground vibration and air movement is essential to reduce the noise of the measure. We adopted a passive pneumatic table (BM-10 bench top vibration isolation platform, by Minus K Technology) and an acoustic enclouser (a $510 \times 655 \times 720$ mm cage provided by Park Systems)

A second instrument, a KLA-Tencor P-16+ profilometer, absolves the same task on a larger scale. The instrument, shown in fig. 5.8, is a contact profilometer, that uses a diamond stylus pressed on the sample and then moved laterally across the sample for a specified distance and specified contact force. It can measure small surface variations in vertical stylus displacement as a function of position. The height position of the diamond stylus generates an analog signal which is converted into a digital signal, stored, analyzed, and displayed. Its scans can be 200 mm long and have a vertical resolution of a few nanometers, with a vertical range of 1 mm. In this case the tip is pressed against the surface by a spring, applying on the sample forces between 0.5-50 mg and registering force variation on a topographical image, that can be 2D or 3D. The stylus radius is 2 μm and horizontal resolution is controlled by the scan speed (1-5000μm/s) and data signal sampling rate (1-1000 Hz). This instrument is less precise than AFM but is useful for determination of layer thicknesses.

Figure 5.8. KLA-Tencor profilometer

5.4 Annealing facility

The last part of my work required heating of the Al/MgF_2 mirrors under vacuum conditions. A tubular oven connected with a pumping system supplied by

the physics department of the university of Padova completed the process. The heating by graphite resistance could obtain temperatures up to 900℃, well beyond those necessary for my experiment. Pressure was some 10^{-5} mbar.

Chapter 6

Monolayer deposition

The first part of the experimental work focused on the understanding of the response of the deposition facility to changes in deposition parameters. To obtain the desired output, it was necessary to calibrate the microbalance, increasing the accuracy on the final thickness, and to explore the characteristics of the deposited layers for various deposition conditions.

Several samples were produced in the e-beam facility, depositing layers of Al and MgF_2 with different characteristics on monocrystalline Si wafers (0.7 mm thick cut along the (100) plane). Base pressure was on the order of 10^{-6} mbar.

6.1 Control of morphology according to deposition conditions

As already outlined in 4.2 the morphological and structural characteristics of the deposited layers depend on the deposition conditions, namely deposition rate and substrate temperature. Images taken with the AFM show the flatness of the surface, indicating the root mean squared roughness (R_q), which is also an important parameter that influences specular reflection. Dimensions of the superficial grains are also linked to growth mechanisms and microstructure.[54, 55]

The AFM images I have taken on the samples, scan an area of $2\mu m \times 2\mu m$ with a resolution of 512×512 pixels. Fig. 6.1 shows two representative images taken for the two materials. Even with a qualitative look the differences in the characteristics of the materials are clear. For MgF_2 it is easy to obtain a fine grained structure, with small roughness; for Al instead, films tend to grow forming bigger island, causing increase in roughness.

To obtain a more detailed comprehension of these processes is useful to compare the values of roughness of the samples and plot them as a function of deposition conditions (temperature and deposition rate). The investigated samples have a

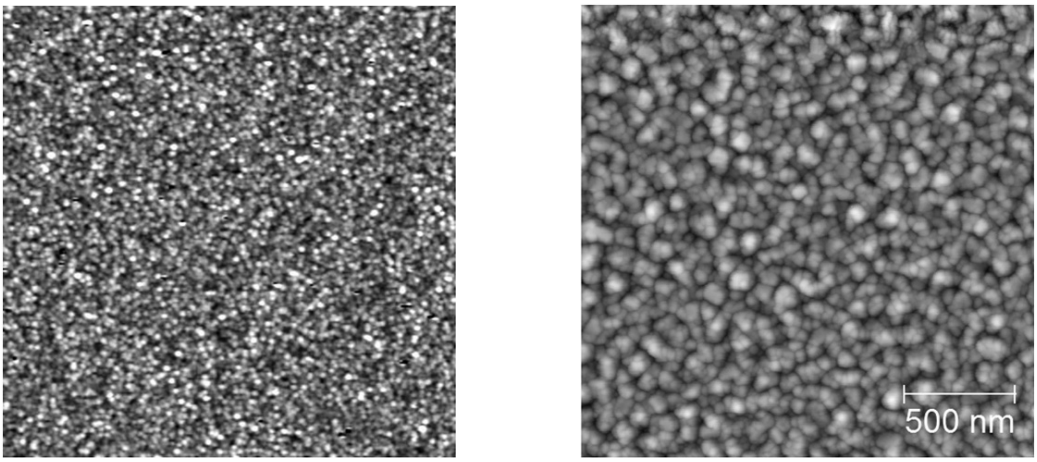

(a) MgF_2 (b) Al

Figure 6.1. Morphological differences between MgF_2 and Al layer deposited by evaporation. Presence of bigger grains and higher roughness in Al is shown

thickness of 100 nm and were deposited at temperatures ranging from 100℃ and room temperature, and with deposition rates from 0.5 Å/s to 30Å/s.

Magnesium fluoride

Fig. 6.2 shows that there is little variation in the roughness of MgF_2 for the ranges of temperature and deposition rate analyzed. The morphology indicates presence of a fine grained structure, with good flatness and roughness inferior to the nanometer. This is in accord to the structure zone model, that foresee this type of growth for dielectric materials at temperatures lower than $0.3T_M$, where T_M is the melting point of the material (1263℃ for MgF_2).[54]

Publications focused on this material have analyzed more thoroughly the characteristics of evaporated MgF_2 thin layers and discovered that, due to low mobility of adatoms, growth is columnar, with shadowing effects that create a porous structure, lowering the packing density of the film and facilitating absorption of impurities.[56]

Aluminum

Fig. 6.3 shows that for Al, like for most metals, to obtain a fine grained structure with low roughness, deposition must be fast and at room temperature. A fast deposition facilitates nucleation of many grains, which do not have the time to grow and form larger structures. A room temperature substrate blocks the adatoms in their landing positions, preventing their diffusion and formation of bigger grains.

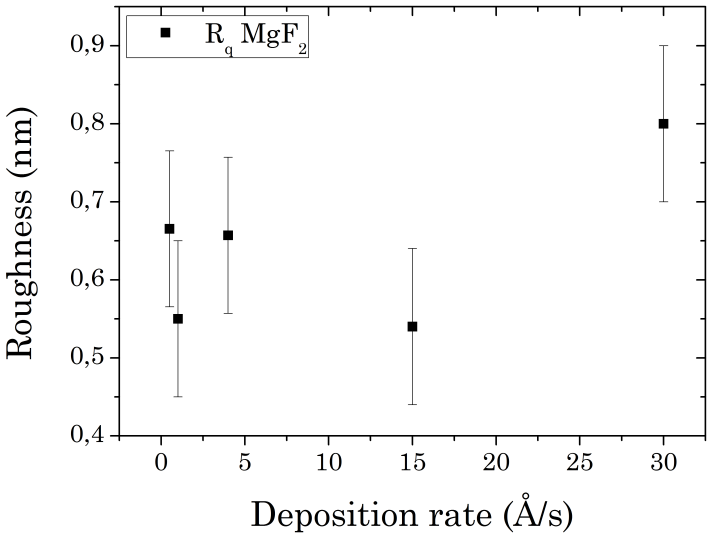

(a) MgF_2 layer roughness as a function of deposition rate

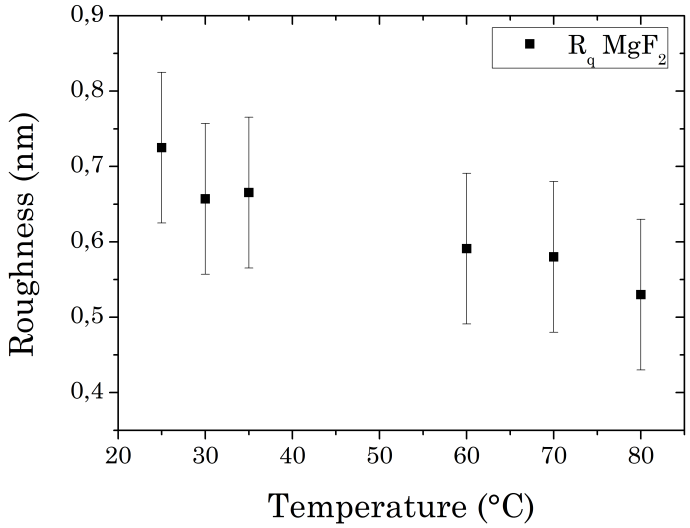

(b) MgF_2 layer roughness as a function of substrate temperature

Figure 6.2. Roughness of MgF_2 samples deposited at different deposition rate (a) and substrate temperature (b). Very low surface modifications occur.

For this material, attention to deposition conditions is particularly important, since the differences in the final roughness values are big and easily lead to unacceptable results.

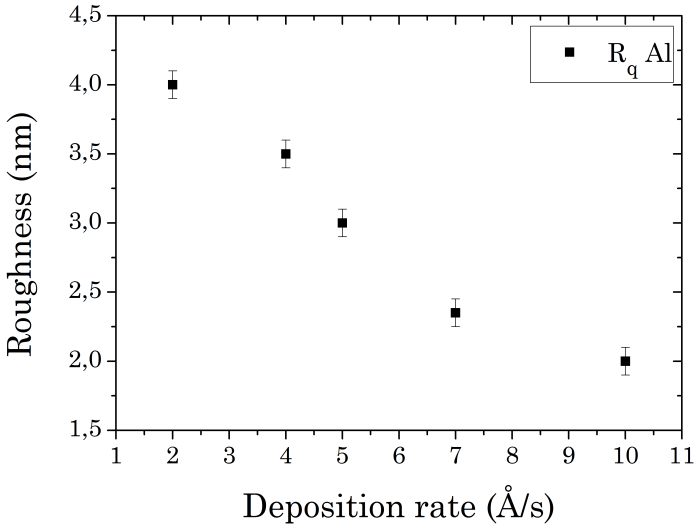

(a) Al layer roughness as a function of deposition rate

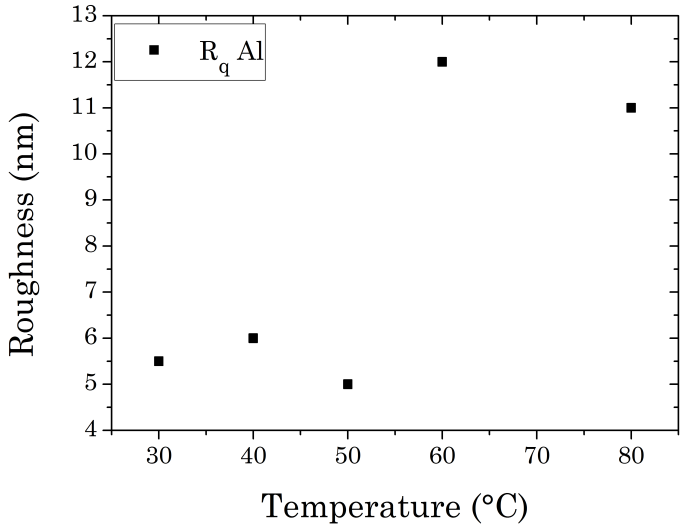

(b) Al layer roughness as a function of substrate temperature

Figure 6.3. Roughness of Al samples deposited at different deposition rate (a) and substrate temperature (b). Roughness values decrease for higher deposition rates and for depositions at room temperature.

6.2 Thickness calibration

The Inficon quartz microbalance calculates the thickness of the depositing layer by registering variations in the oscillation frequency of the crystal. Those variations are due to the added mass deposited on the crystal surface with the evaporated

material. Discrepancy from the thickness values thus calculated and those measured with the profilometer are due to uncertainties on the density of the film, that is usually different from the bulk values reported in literature, and to the fact that the deposition is not uniform all over the chamber, which causes the flux of evaporated materials to be different on the sample and on the crystal surface. It is possible to calculate, with some testing deposition, an approximate material density and geometric factor to compensate this error, but to obtain a good prediction of the final thickness, the use of a calibration line is essential.

Fig. 6.4 and 6.5 show the calibration lines for the two deposited materials. The deposition parameters were those found to be optimal in the previous section. To obtain the curves, different deposition were made with nominal thickness values around the desired thickness output (700 Å for Al and 250 Å for MgF_2). The fitting curve is a straight line.

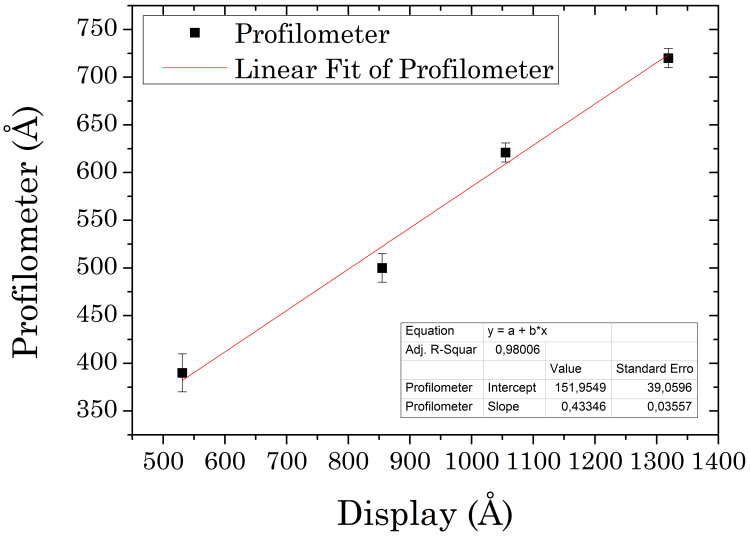

Figure 6.4. Calibration curve for Al depositions

Precision of Al layer thickness is not a stringent requirements, since for thicknesses superior to 700 Å its reflectivity remains constant. The thickness of the capping layer, on the other hand, is crucial to obtain maximum constructive interference. For this reason MgF_2 calibration was the more accurate of the two.

6.3 Spatial uniformity of deposition

Since the crucible is, compared with the dimensions of the evaporation chamber, small , and since its material emission is not expected to be uniform in all directions, the final thickness of the deposited layer will depend on the positioning of the

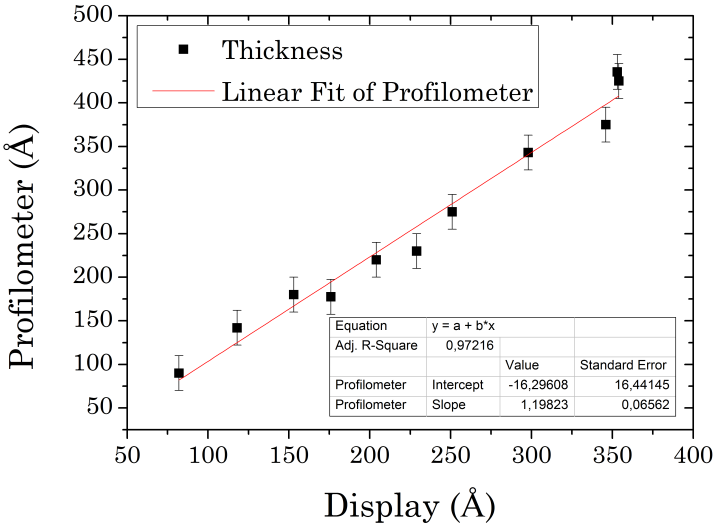

Figure 6.5. Calibration curve for MgF_2 depositions

substrate. Substrate samples are positioned, facing down to the target, on the bottom face of a disc that can rotate around its center. The emission from the crucible is greater for directions close to the normal, so increasing the radial distance (r) of the sample from the center of the disc will result in thinner films. Even for a fixed value of r, thicknesses of samples positioned at different angles (ϑ) will be different.

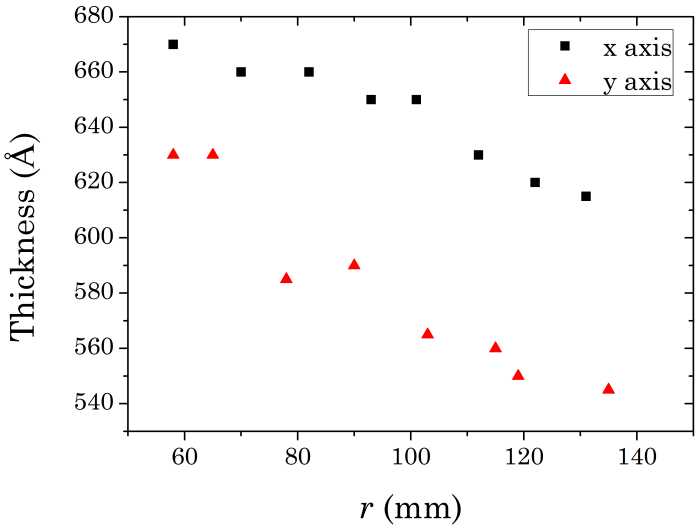

Figure 6.6. Thicknesses of layer deposited in different position in the chamber. Deposition is thicker near the center, with a decreasing trend towards the outer areas. Deposition thicknesses vary also considering different angular positions.

Fig. 6.6 shows variations in thicknesses for substrates positioned in different point

of the chamber. r is measured in mm from the center of the disk, the decreasing trend at greater distances from the center is clear. The two curves represent depositions in two directions perpendicular to each other ($\vartheta(x) = \vartheta(y) + 90°$). The differences for different directions are significant, around 10%. Discrepancies in the ϑ direction are compensated rotating the substrate holder disk, those relative to r position cannot be eliminated and pose a limitation to the dimensions of the samples that can be realized in this facility.

A comparison of different depositions, implemented with rotating substrates, shows a plateau in the thicknesses values around $r = 80$ mm, which is chosen as the preferential position of the substrates. In fig. 6.7 are reported the thicknesses of those depositions, their values normalized to the unity at $r = 80$ mm. From the graph we can estimate a uniformity of $\pm 5\%$ in the region between $r = 45$ mm and $r = 120$ mm. This region, 75 mm wide, represents the maximum width of the samples that can be deposited with this facility, unless more stringent requirements are specified.

The graph contains thicknesses from both the materials concerned by this work. They assume different shapes while melting in the crucible, MgF_2 maintains the granularity of its pieces, melting only the outer layers, while Al forms a fluid that wet the surfaces of the crucible. This difference could lead to differences in thickness distribution; as seen in the figure, they are not substantial, if not for the higher values of r, where Al tends to decrease its thickness more promptly.

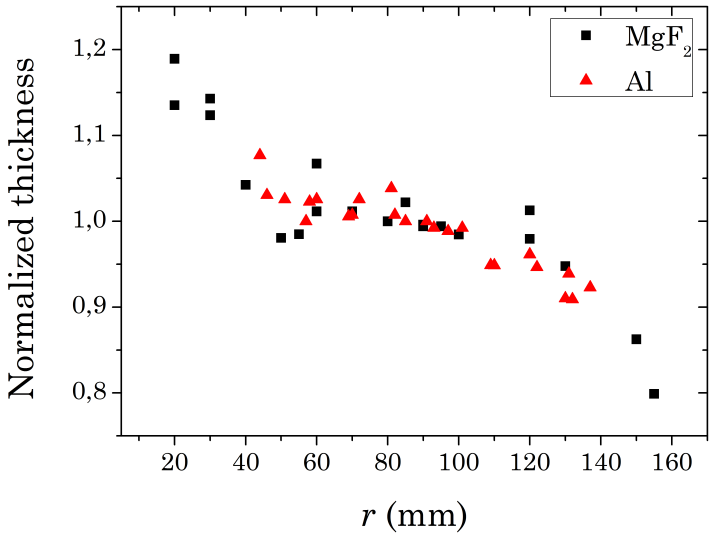

Figure 6.7. Normalized thicknesses of layers deposited in different positions in the chamber. Good uniformity for both materials is granted in the section with 45 mm $< r <$ 120 mm.

Chapter 7

Optical characterization

The optical behavior of Al and MgF_2 is well known. Accurate data on their optical constant in the VUV is available in literature.[57] However, this data refer to bulk materials; when considering thin films the situation changes. As seen in section 6.1, the final output of a deposition can change greatly according to deposition conditions, and this reflects on the optical properties of the product. To control the quality of the work and to predict the efficiency of the device a better undersatanding of the optical properties of the layer produced with our facility is necessary. For Al the deposition method converged early on the "fast and cold" process, producing layers whose optical quality was comparable between various authors.[58–60] Furthermore, determination of optical constants of Al is a problematic task, since the oxide layer that forms shortly after deposition modify the results. Since in our deposition facility instrumentation for the optical analysis is not embedded, it was not possible to determine the optical quality of the deposited Al without the bias of the passivation layer. For this reason in all the simulations made during my work, I had to resort to the published values.

For MgF_2, results are very different between papers, and it is not straightforward to correlate those changes to their physical causes.[50, 56, 61–63] Fig. 7.1 proves this very well, showing optical constants retrieved from the works of various authors.

It is evident that to obtain reliable optical parameters for our samples the only way was to calculate them experimentally. I prepared for this purpose two samples, MgF_2_A and MgF_2_B, whose characteristics are listed in table 7.1.

The two samples were deposited at optimal deposition conditions. The first (MgF_2_A) was deposited at room temperature, the temperature foreseen for mirrors depositions, the second (MgF_2_B) with the substrate heated at 200℃, the temperature that should give the best quality MgF_2 film. The nominal thickness of the two films (that measured by the microbalance) was the same. The difference in the thickness values measured with the profilometer for the two samples indicates an increased density of the layer deposited at higher temperature, as expected for

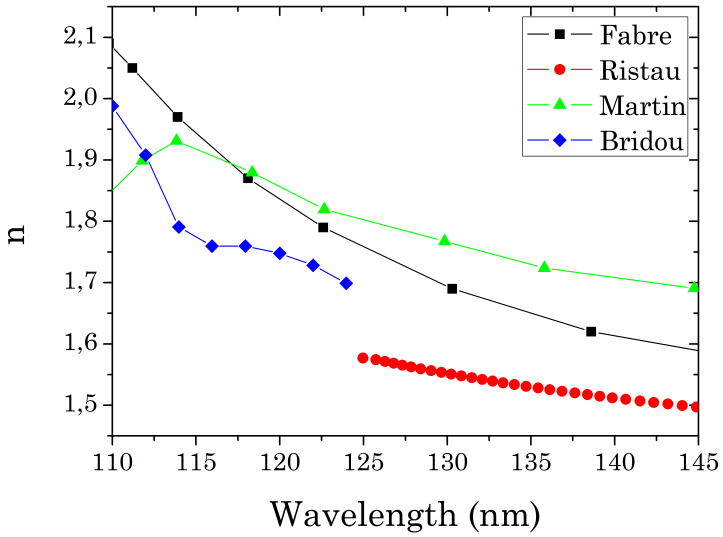

(a) Refractive index of MgF_2 for various authors

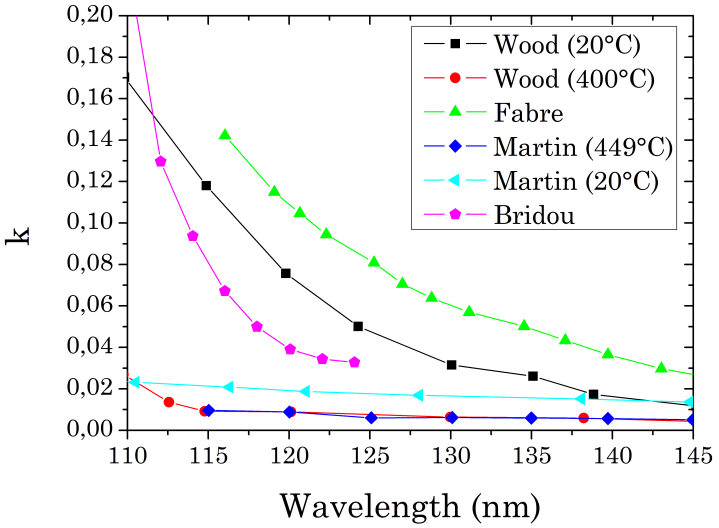

(b) Extinction coefficient of MgF_2 for various authors

Figure 7.1. Optical constants calculated by various authors for MgF_2 thin films. The obtained values vary between them according to variations in the experimental setup and deposition conditions

this material.[45, 46] At BEAR I tested their reflectivity in the wavelength range 8.5-11 eV (112.7-145.4 nm), for different incidence angles. Measurements were repeated for two configurations of the experimental chamber, s and p, corresponding to two opposite polarization states of the incoming beam. The two results were then averaged to obtain reflectivity of the samples in condition of unpolarized light

Table 7.1. Characteristics of samples MgF_2_A and MgF_2_B

Parameter	MgF_2_A	MgF_2_B
Deposition temperature (℃)	25	200
Deposition rate (Å/s)	4	4
Thickness (nm)	72	61
Roughness (nm)	0.72	0.65

(fig. 7.2).

The program IMD (developed by David Windt[64]), allows the determination of the optical constants of a given structure from reflectivity measurements at various incidence angles. The parameters needed are:

- Physical parameters of the structure
  - MgF_2 25 nm, R_q = 0.7 nm;
  - Si substrate, R_q = 0.25 nm;
- Incoming light parameters
  - polarization: p = 0;
  - Incidence angle: scan between 5-80° at fixed wavelength;
  - Wavelength: fixed, measurements repeated for different wavelengths between 112.7-145.4 nm
- Optical parameters of the substrate (indicated by Palik [57])

Then, a least-squares curve fitting procedure finds the values of n and k which best fit the experimental reflectivity. IMD offers 4 types of algorithms for fitting optimization, I chose a genetic algorithm for FOM minimization inspired by the approach described by Binda and Zocchi in [65]. The couples of optical constants this way generated for each wavelength are shown in fig. 7.3.

This values of n and k experimentally obtained well describe the optical behavior of MgF_2 deposited during this work and have been taken into account in the next steps to help foresee and improve the final performances of the product.

Fig. 7.3(b) is particularly interesting, because it shows the difference in terms of absorbance between the two samples. As already explained, deposition at room temperature creates a MgF_2 film filled with defects, with a porous structure that doesn't preserve the optimal transparency of the material. Deposition at higher

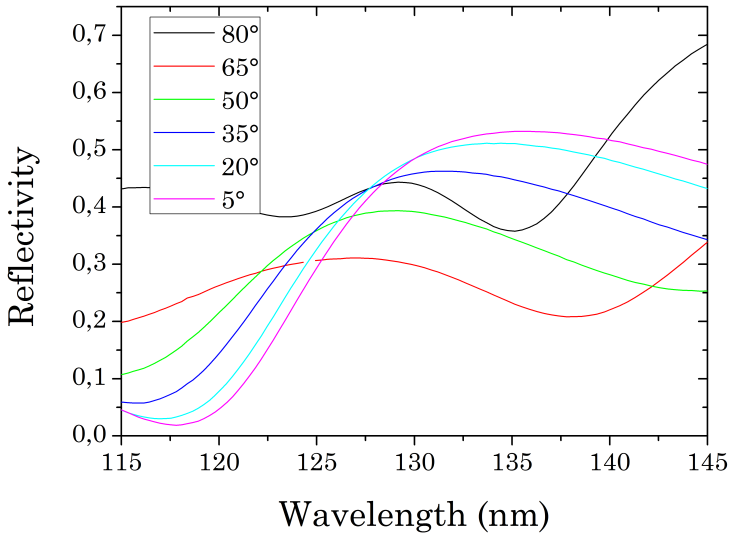

(a) MgF_2_A

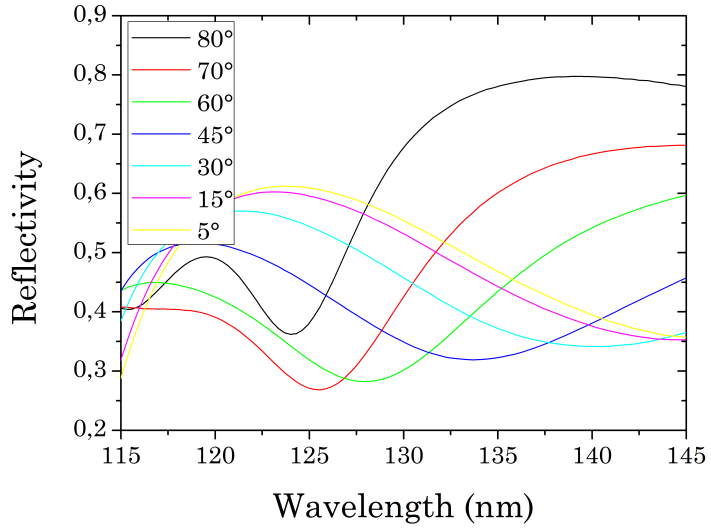

(b) MgF_2_B

Figure 7.2. Reflectivity measurements for the two MgF_2 monolayers deposited at room temperature (a) and at 200℃ (b). Reflectivity in the range 110-145 nm at various incidence angle for unpolarized light is shown.

temperature helps avoiding these problems and the improvement is shown quantitatively in this graph: the extinction coefficient at 121.6 nm decreases from 0.11 (for MgF_2_A) to 0.03 (for MgF_2_B).

Fig. 7.3(a) shows that MgF_2 absorption edge is shifted towards longer wavelengths when the film is deposited at room temperature. The refractive index shows

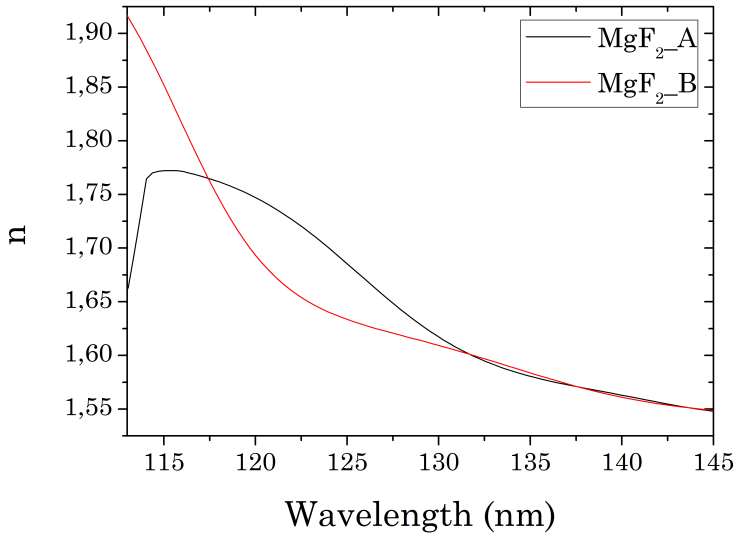

(a) Refractive index

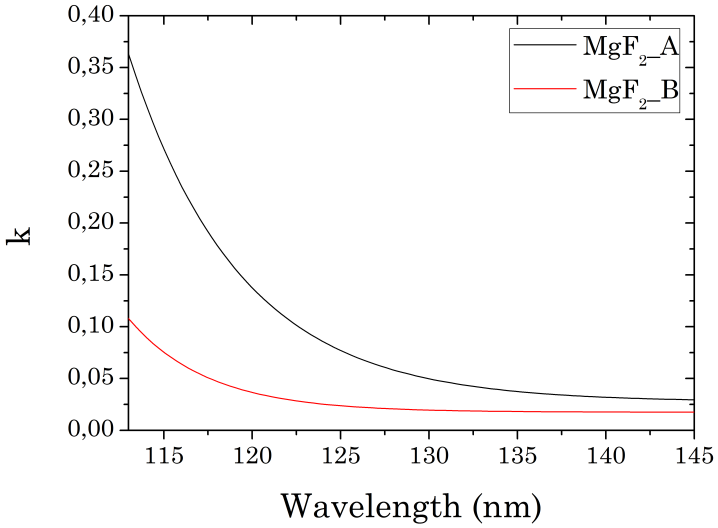

(b) Extinction coefficient

Figure 7.3. Optical constants of the two samples MgF_2_A and MgF_2_B in the range 110-145 nm. The former presents bigger absorption, as shown by the higher values of k, and the absorption edge shifted at longer wavelengths, as shown by the anomalous dispersion of n around 115 nm.

in fact around 115 nm the anomalous dispersion that typically occurs in correspondence with absorption peaks. That feature is instead absent for the sample deposited on heated substrate.

Chapter 8

Mirrors

The following obvious step was to apply the knowledge acquired on materials and processes to the realization of finite optical elements for the VUV. The structure of mirrors for this wavelength region is simple enough, two layer deposited in rapid succession, an Al film first and the MgF_2 capping layer shortly after.

8.1 Process optimization

The deposition method, accepted by the state of the art and confirmed by my previous tests, consisted on a deposition of the Al layer at room temperature, with a deposition rate of 30 Å/s.[45] The deposition rate was a compromise between the capability of the facility, in terms of thickness control and uniformity, and the need of a fast deposition to avoid incorporation of oxygen in the structure. The deposition of the second MgF_2 layer was made at 4 Å/s and at room temperature. On the substrate holder I placed 3 silicon substrate samples. Table 8.1 summarizes the characteristics of the first deposition of Al/MgF_2 mirrors operated in our evaporation chamber (labeled from now on Al/MgF_2_A).

Adopting these parameters I deposited 3 mirrors with similar characteristics with a best reflectivity at 121.6 nm of 71.5%. The gap between this product and those available on the market (a 10% difference in reflectivity) could be explained by three critical points:

1. Cleanliness of the deposition chamber;
2. Deposition rate;
3. Pressure in the chamber.

Table 8.1. Deposition characteristics of Al/MgF_2_A mirrors

Parameter	Al/MgF_2_A
Chamber pressure (mbar)	$1.9 \cdot 10^{-6}$
Deposition temperature, Al (℃)	25
Deposition temperature, MgF_2 (℃)	25
Deposition rate, Al (Å/s)	30
Deposition rate, MgF_2 (Å/s)	4.5
Nominal thickness, Al (nm)	63.5
Nominal thickness, MgF_2 (nm)	24.5
Sample's 1 reflectivity (%)	71.5
Sample's 2 reflectivity (%)	71.3
Sample's 3 reflectivity (%)	71.4
Sample's 1 measured thickness (nm)	87
Sample's 2 measured thickness (nm)	87
Sample's 3 measured thickness (nm)	84

I tried to address these three aspects to improve the performances. In the following I will analyze each point separately, explaining it and describing the solution I tried to apply.

Cleanliness of the deposition chamber

In the evaporation facility used during this work, were carried on several experiment concurrently, involving different materials (Au, Pd, SiO_2, ...). For this reason the cleaning of the surfaces of the chamber, contaminated with impurities of unwanted metals and oxides, was a fundamental part of the deposition process. An ordinary cleaning procedure consisted in rubbing with a cloth soaked with isopropyl alcohol (IPA) or acetone. This process was not strong enough to remove all the impurities and the layers deposited on the walls. A more thorough process was then applied, dismounting the various parts of the facility and brushing them with a rotating brass wire brush actuated by a drill.

This process could bring to light the steel surfaces of the facility, eliminating most of the contamination. The pressure levels reached by the chamber and its pumping down time improved considerably, proving the effectiveness of the method.

Deposition rate

Literature data indicate that reflectivity of mirrors in the VUV starts to decrease if the deposition rate is slower than 100Å/s, the higher the pressure in the chamber

during deposition, the higher the loss.[42] For our setup, that cannot reach UHV conditions, the possibility to increase the deposition rate from the 30Å/s of the first depositions to those values would be an important improvement. This contrasts with the optimal operational mode of the facility, for various reasons. At high deposition rates, the delay present when opening and closing of the shutter makes impossible to have an accurate control of thickness, the rotation of the substrate holder becomes too slow to guarantee the lateral uniformity of the deposited layer, the intensity of the electron beam, concentrated on a small crucible, makes the fused material unstable.

To verify the importance of this considerations on the quality of the final films, I deposited two Al single layers, 85 nm thick, at two different deposition rates: (Al_A) 30 Å/s and (Al_B) 60 Å/s. The roughness measured with AFM was 1.3 ± 0.1 nm for Al_A and 1.4 ± 0.1 nm for Al_B. The reflectivity was tested above 200 nm, where the Al_2O_3 layer doesn't influence the results, with the Cary spectrophotometer. Table 8.2 shows the characteristics of the two depositions and of the obtained monolayers.

Table 8.2. Characteristics of Al monolayer deposited at a rate of 30Å/s and 60Å/s

Parameter	Al_A	Al_B
Chamber pressure (mbar)	$8 \cdot 10^{-6}$	$7.6 \cdot 10^{-6}$
Deposition temperature (℃)	25	25
Deposition rate (Å/s)	29	60
Nominal thickness (nm)	112	136
Mean reflectivity [200-600 nm] (%)	81.35	54.71
Measured thickness (nm)	83.5	86.5
Roughness (nm)	1.3	1.45

Fig. 8.1 shows the results, obtained in the 200-600 nm wavelength range, and compared with a theoretical simulation made with IMD software. Sample Al_A confirms the 10% discrepancy with the state of the art already measured at 121.6 nm. Sample Al_B has a clear decrease in reflectivity, with a drop for shorter wavelengths to values lower than 40%. These results suggested to give up the efforts to increase the deposition rate and focus on other deposition aspects.

Pressure in the chamber

After the cleaning process, the pressure in the chamber at the beginning of the deposition was $2{\cdot}10^{-6}$ mbar, this level of vacuum obtainable after several hours of pumping. It is already clear that a better vacuum level is beneficial to the quality of the deposition, so it was important to work in that direction.

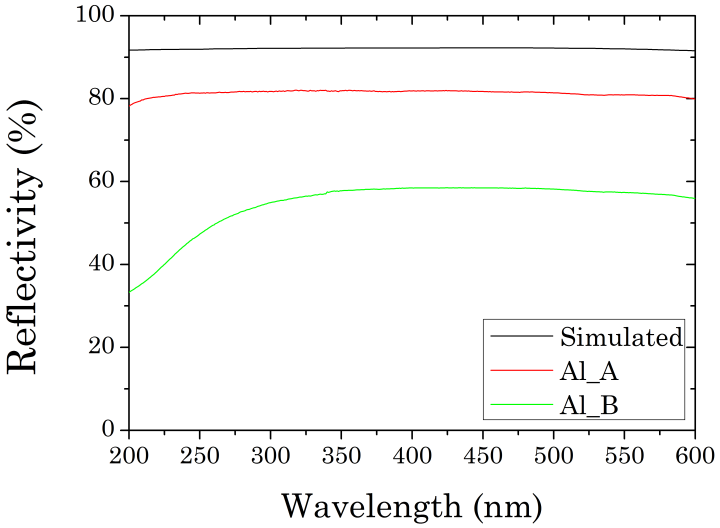

Figure 8.1. Comparison between Al layers deposited with deposition rates of (Al_A) 30 Å/s and (Al_B) 60 Å/s. An important loss of reflectivity occurs for the sample deposited at the higher deposition rate

It is typical for vacuum systems to increase the vacuum level with getter materials, that adsorb or bind chemically the gases present in the chamber to reduce their presence in the mixture and avoid desorption from the walls.[66] For our system titanium metal, evaporated by the electronic beam before the actual deposition, acted as getter for O_2 and H_2O molecules, lowering the pressure to $2{\cdot}10^{-7}$ mbar, one order of magnitude lower than before. Optimal parameters for Ti deposition are: rate of 1 Å/s, room temperature, 100 nm thickness.

Table 8.3. Characteristics of new deposition of Al/MgF_2_B mirrors

Parameter	Al/MgF_2_B
Chamber pressure (mbar)	$3.2 \cdot 10^{-7}$
Deposition temperature, Al (℃)	25
Deposition temperature, MgF_2 (℃)	25
Deposition rate, Al (Å/s)	20
Deposition rate, MgF_2 (Å/s)	2.5
Nominal thickness, Al (nm)	64
Nominal thickness, MgF_2 (nm)	24.7
Best sample's reflectivity (%)	75.8

Applying the listed precautions, I deposited new mirrors (Al/MgF_2_B). Table 8.3 lists the characteristics of the deposition and the best reflectivity obtained

among the 8 samples thus deposited. I found, thanks to the new adaptations, an increase in performances, shown in fig. 8.2. The new reflectance values reached a maximum of 75.8% at 121.6 nm. This value is still lower than published results, but the improvement was more than 4%, halving the gap.

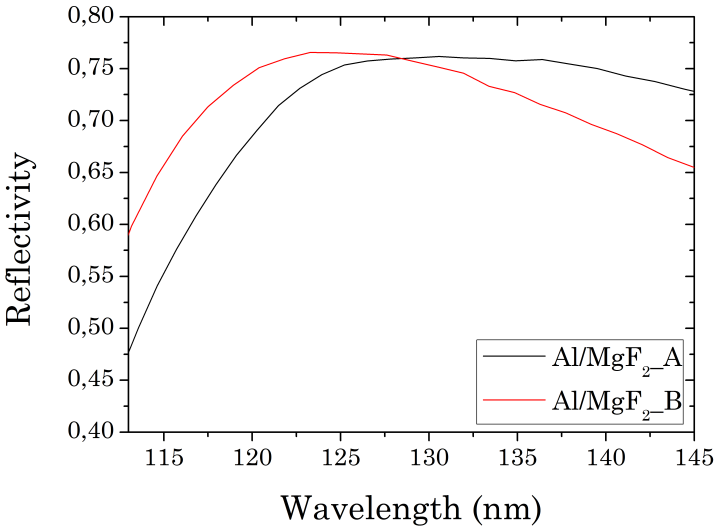

Figure 8.2. Comparison between Al/MgF_2 mirrors deposited before and after optimization of the process. The correct adjustment of all the deposition parameters allowed for an increment in reflectivity of 4% at 121.6 nm.

8.2 Effects of temperature

The deposition at room temperature preserves the reflective quality of Al, but causes a certain amount of absorption in the MgF_2 layer. In fact, as explained in section 6.1, the structure of the film is porous and absorbs oxygen and humidity from air. A less absorbing structure is obtainable depositing the film on a substrate heated over 200°C. Several publications attested this behavior, attributing it to the formation of a structure with bigger grains[62], with preferred orientation[50] and with a more closely packed structure[46]. Experimental determination of extinction coefficient for MgF_2 deposited at room temperature and at 200°C shown in section 7 confirms the trend.

As explained by Hutcheson[45], attempts at depositing optical coatings at high substrate temperature were unsuccessful. Heating of the substrate can in fact improve the performances of the capping layer, but it also confers to Al a layer structure that present bigger grains, high roughness and consequently lower reflection. A possible alternative I explored to preserve the qualities of both the material was the adoption of a 3 steps process:

1. Deposition of the Al layer at room temperature;
2. Increasing of the temperature of the substrate to 100℃;
3. Deposition of the MgF_2 layer on a heated substrate.

According to [48] an annealing at 100℃ will not produce the growth of larger Al grains that is so detrimental to the final reflectance. The sample thus produced (Al/MgF_2_C) was compared with Al/MgF_2_A , which was deposited at similar conditions but without the heating step. Table 8.4 shows the differences between them.

Table 8.4. Comparison between mirror with capping layer deposited at 100℃ (Al/MgF_2_C) and mirror deposited entirely at room temperature (Al/MgF_2_A)

Parameter	Al/MgF_2_A	Al/MgF_2_C
Chamber pressure (mbar)	$1.9 \cdot 10^{-6}$	$1.9 \cdot 10^{-6}$
Deposition temperature, Al (℃)	25	25
Deposition temperature, MgF_2 (℃)	25	100
Deposition rate, Al (Å/s)	30	25
Deposition rate, MgF_2 (Å/s)	4.5	5
Nominal thickness, Al (nm)	63.5	67
Nominal thickness, MgF_2 (nm)	24.5	24.5
Reflectivity (%)	71.5	64.2
Measured thickness (nm)	87	94.5

The results, visible in fig. 8.3, were unsuccessful and the reflectance at 121.6 nm dropped from 71.5% to 64.2%.

The reason for this decrease could be due to partial rearrangement of the grain structure of the film, hypothesis supported by the increased roughness of the sample (R_q = 1.8 nm from AFM measurements, 0.4 nm more than samples deposited at room temperature). Another explanation foresee the formation of the oxide layer on top of the Al film during the time needed to heat the substrate. Even if the process take place in the high vacuum of the evaporation chamber, the thickness of Al_2O_3 sufficient to ruin the performance is so small that this is a likely scenario.

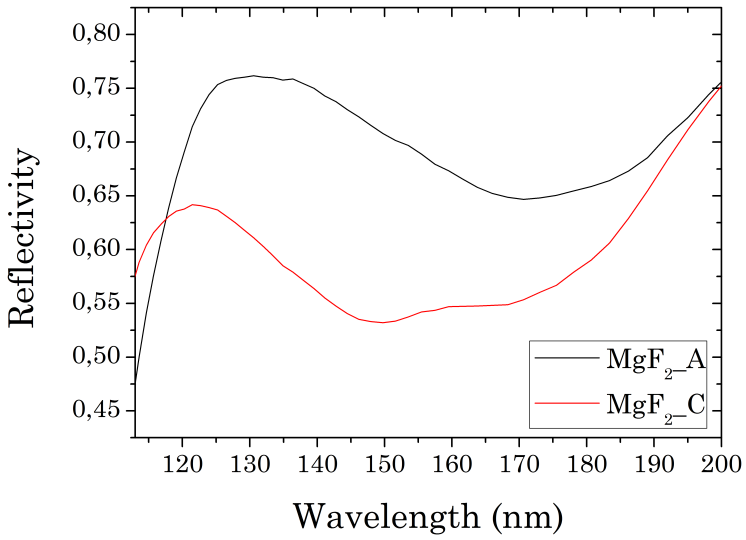

Figure 8.3. Comparison between Al/MgF_2 mirrors deposited at room temperature (Al/MgF_2_A) and with the 3 steps heating process (Al/MgF_2_C). The Al layer degrades even in the high vacuum of the deposition chamber when heated, the resulting mirror has lower quality optical properties.

Chapter 9

Annealing

Having failed all the efforts to deposit a hot, not absorbing MgF_2 layer, the option left is a successive annealing of the completed structure. This process could obtain a reordering of the porous structure of the upper layer towards a more compact film, similar to that of hot substrate deposition.

In 1970, Adriaens deposited Al/MgF_2 mirrors at room temperature and annealed for 60 h at 300℃. Depositions were made at an initial pressure of 2×10^{-10} torr from tungsten or platinum boats and the annealing carried on using a heater built onto the substrate holder at a pressure of 10^{-7} torr. The annealed films showed increased reflectance for wavelengths lower than 125 nm and some decrease in reflectance at longer wavelengths. The thickness of the deposited samples was 15 nm, for this reason the absolute reflectance values are not comparable with other results, remaining lower than those obtainable with the 25 nm thickness that optimize reflectivity at 121.6 nm.[67]

Only more recently, in 2007, Fernández-Perea returned on the subject, suggesting annealing as a possible way to improve performances of VUV mirrors. According to her paper, Al can withstand annealing at 270℃ for 1 h without degradation in an UHV environment, and annealing at 250℃ of Al/MgF_2 mirrors doesn't degrade the structure.[48]

Apart from these two contributions, this technique seems to be still unexplored. The next sections are dedicated to the study of annealing effects on MgF_2 and on Al/MgF_2 bilayers. Times and temperatures are valuated and the effects on the optical properties analyzed.

9.1 Annealing of MgF_2 monolayers

As a preliminary step I studied the behavior of the capping layer material, to verify if a real enhancement of the optical properties take place after heating. To do so I first

deposited a series of samples in the e-beam chamber, 35 nm thick MgF_2 monolayers on Si substrate, deposited at room temperature and with a deposition rate of 4 Å/s. Table 9.1

Table 9.1. Deposition characteristics of MgF_2 monolayer deposited to study the annealing process

Parameter	MgF_2
Chamber pressure (mbar)	$5 \cdot 10^{-6}$
Deposition temperature (℃)	25
Deposition rate (Å/s)	3.5
Nominal thickness (nm)	35

Annealing of these samples took place in air, on a hotplate that can operate between 300 and 500℃. Samples remained on the heater for different periods of time and at different temperatures, to verify the differences of annealing effects at different conditions. After treatment, verification of optical performances occurred in the normal incidence reflectometer, measuring the reflectivity of the samples at 121.6 nm and at 45°. Fig. 9.1 shows the obtained reflectivity as a function of annealing times and at two different annealing temperatures, 300℃ and 350℃.

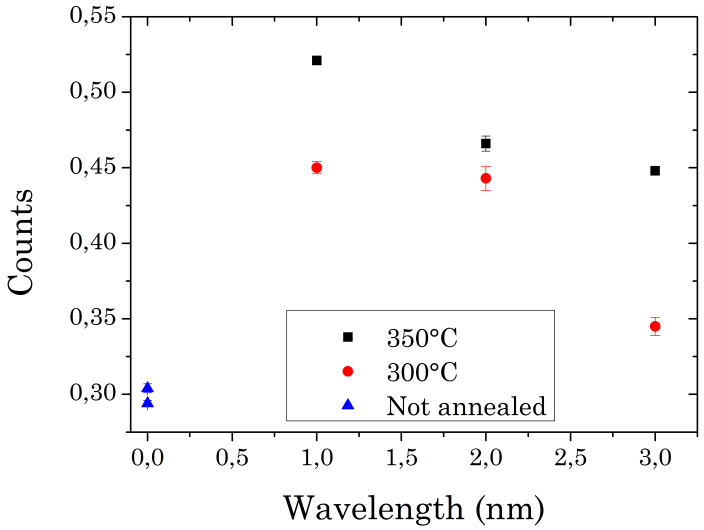

Figure 9.1. Reflecivity of MgF_2 samples annealed at 300℃ and 350℃. Annealing provides an increased reflectance, best results are obtained for 1 h annealing time and 350℃ annealing temperature.

From this first run of measurements i found that there is an actual increment in reflectivity after the annealing process. The effect is maximized for short annealing times and is greater at the temperature of 350℃.

Since in the first run the higher temperature used gave the best results, a second run was made, increasing it further to 400°C. Table 9.2 lists the parameters of this deposition. This change produced, as shown in fig. 9.2, the loss of the beneficial effects present for annealing at lower temperatures. Only a small gain in reflectivity remained.

Table 9.2. Deposition characteristics of MgF_2 monolayer deposited to study the annealing process at higher temperature

Parameter	MgF_2
Chamber pressure (mbar)	$6 \cdot 10^{-6}$
Deposition temperature (°C)	25
Deposition rate (Å/s)	4
Nominal thickness (nm)	35.4

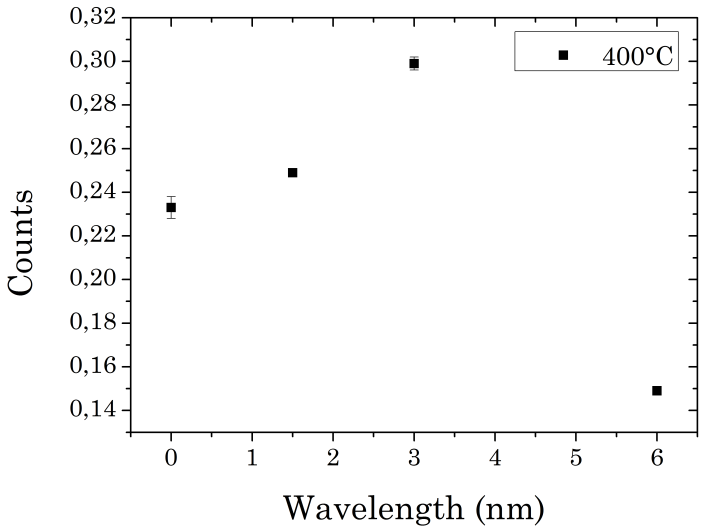

Figure 9.2. Reflecivity of MgF_2 samples annealed at 400°C. Results are not satisfying as those obtainable with annealing at lower temperatures.

From this preliminary analysis it appears that MgF_2 well reacts to heating, reducing its absorption considerably. At the best annealing conditions (350°C for 1 h) the reflectivity was 52%, 22% more that the reflectance of "cold" samples.

9.1.1 Thicknesses

The annealing process should have the effect of transforming the structure of the layer, changing a porous columnar structure with density values lower than bulk

ones, to a more compact packing with densities similar to bulk. This should inevitably lead to a shrinking of film thickness. To verify this assumption thicknesses of the MgF_2 samples were measured before and after heating with the profilometer. Table 9.3 shows the results.

Table 9.3. Changes in thickness for annealed MgF_2 samples

Sample	Annealing temperature (℃)	Annealing time (h)	Thickness as deposited (nm)	Thickness after treatment (nm)	Thickness change (%)
1	300	1	37	36.2	-2.16
2	300	2	35.5	36.5	+2.82
3	300	3	38	36	-5.26
4	350	1	37.5	34.5	-8
5	350	2	37.5	35	-6.67
6	350	3	36.5	35.5	-2.74
7	400	1.5	43.5	41.5	-4.6
8	400	3	40	37	-7.5
9	400	6	41.5	41	-1.2

As expected, the annealing parameters that give the best reflectivity increase provide also the biggest difference in density of the layer (-8% in thickness for the sample annealed for 1 h at 350℃). For annealing at 350℃ and 400℃, reflectivity trends and thickness variations trends, as a function of annealing time, have the same shape, confirming that density variation is a crucial parameter to verify the effectiveness of the process. Remains unclear why an increase in annealing time results in both lowered reflectivity improvement and lower thickness change and why annealing at 400℃, even when providing a good density increase, doesn't result in good reflectivities. Greater absorption of O_2 from atmosphere, due to higher temperature or higher exposure times, is the most probable explanation. For annealing at 300℃ instead, variations in thickness are lower and I could not find a clear trend.

Considering Al monolayers, heating facilitates the oxidation process, and this is clearly visible with the naked eye, since the appearance of the coating changes from shining silvery to an opaque white. Regarding thickness variations, they are summarized in table 9.4.

In this case there is no increase in the packing density, on the contrary the effect seems to be a small increase in thickness; compatible with a change in the structure towards formation of bigger grains, expected effect for Al at high temperature[48]. This confirms the fact that MgF_2 protection is necessary for treatment of Al at high temperatures.

Table 9.4. Changes in thickness for annealed Al samples

Sample	Annealing temperature (℃)	Annealing time (h)	Thickness as deposited (nm)	Thickness after treatment (nm)	Thickness change (%)
1	300	1	62.5	63	+0.8
2	300	2	63	64.5	+2.4
3	300	3	62.5	63	+0.8
4	350	1	61	62.5	+2.46
5	350	2	62.5	63	+0.8
6	350	3	62.5	63.5	+1.6

9.2 Annealing of Al/MgF_2 mirrors

Following the positive results of the previous section, the study continued towards the investigation of annealing effects on mirrors for the VUV. The deposition followed the usual procedure:

- Achievement of a pressure of 10^{-7} mbar
- Deposition of 70 nm of Al at room temperature and with a deposition rate of 30 Å/s
- Deposition of 25 nm of MgF_2 at room temperature and with a deposition rate of 4 Å/s

The obtained samples (Al/MgF_2_D) have the characteristics listed in table 9.5.

Table 9.5. Characteristics deposition of Al/MgF_2_D mirrors

Parameter	Al/MgF_2_D
Chamber pressure (mbar)	$5 \cdot 10^{-7}$
Deposition temperature, Al (℃)	25
Deposition temperature, MgF_2 (℃)	25
Deposition rate, Al (Å/s)	20
Deposition rate, MgF_2 (Å/s)	2
Nominal thickness, Al (nm)	61.5
Nominal thickness, MgF_2 (nm)	24.7

After deposition reflectivity was measured in the normal incidence reflectometer at 121.6 nm at near normal incidence (15°).

After the first measurement the annealing process was carried on. To protect the Al layer from the possibility of oxidation, heating occurred in this case under vacuum conditions. The tubular oven used for the process could reach a vacuum of 10^{-5} mbar and the temperatures explored were 350℃ and 300℃. After treatment new reflectivity measurements were carried on in the normal incidence reflectometer with the same experimental parameters. Table 9.6 lists the results.

Table 9.6. Reflectivity of Al/MgF_2 before and after annealing

Sample	R% as deposited	R% after treatment
Annealed at 350℃ for 1 h	71	71
Annealed at 300℃ for 0.5 h	72	77

The presence of the Al layer limits the impact of the process. At the optimal temperature for MgF_2 annealing, oxidation of Al nullifies the benefits found in the previous section and reflectivity doesn't have great variations. Settling for lower temperatures we still obtained a 5% increment in reflectivity. The value of reflectance before annealing was not comparable with the maximum ever obtained with our facility, so the overall increment in the device performances is 2%.

The quality of mirrors deposited in our facility, after all the optimization processes and annealing cures, is still lower than that commercially available. This is due to unavoidable experimental problem that limit our results, like chamber dimensions and heating capability. The improvements adopted were nevertheless positive, and the annealing study useful for future applications.

Chapter 10

Conclusions

The Al/MgF_2 mirrors produced in this work are the result of an extensive study on the characteristics of facility and materials. To obtain the desired deposition, a preliminary study of the characteristics of the deposition chamber was necessary. Understanding about calibration of the resulting thicknesses, repeatability, spatial disuniformities, is fundamental to tailor the deposition towards the desired output.

The quality of the device is also dependent on the characteristics of the materials used, which, in turn, depend on deposition parameters. I verified that the morphology of the aluminum layer requires fast deposition rates and low substrate temperature to avoid formation of big grains with high roughness. For magnesium fluoride the morphological features are less demanding, with a smooth surface at all conditions, but optical characterization showed how deposition at room temperature results in bigger absorption with respect to deposition on a substrate heated at 200℃.

The control of these parameters was essential, along with the use of best possible vacuum levels and high purity and cleanliness of materials and environment. Aluminum deposition rate was an unsolved limitation, since in this facility was not possible to adopt the higher rates necessary to avoid incorporation of oxygen in the layer with consequent limitation in the reflectivity. Adopting the aforementioned precautions we obtained VUV mirrors with 75.8% reflectivity at 121.6 nm.

The novel approach of this thesis to the realization of mirrors for the vacuum ultraviolet, was the study of the effect of heating processes, at first changing the substrate temperature after Al deposition, to deposit the capping layer at high temperature, but not obtaining good results; then with post deposition annealing processes. Experimentation determined that annealing at 350℃ for period of times up to 1 h increases greatly reflection of MgF_2 monolayer, from 30 to 52% at 121.6 nm at 45°. This effect was present even at lower temperatures and is lost at 400℃. The results were expected but an exact determination of temperatures and times to be used was not clear from the literature.

Application of this process to aluminum layers was more delicate, since the tendency of this material to oxidation and to change its structure when heated. When protected from the magnesium fluoride layer, the Al mirrors could be annealed, obtaining an increase in reflectivity to 77%, but the annealing temperature had to be reduced to 300℃.

This process is not applied in the deposition procedures found in literature, even if it has been suggested or tried on some not optimized samples in a couple of works. Given the not perfect starting quality of the samples on which annealing was realized, it is still not possible to determine if annealing can improve the best reflectivity obtainable with a room temperature deposition, but provided a slight increase of performance for the samples deposited in our facility.

Bibliography

[1] D. K. Lynch and W. C. Livingston. *Color and light in nature.* Cambridge, UK: Cambridge University Press, 2nd edition, 2001.

[2] M. C. Dash and S. P. Dash. *Fundamentals Of Ecology.* Tata McGraw-Hill Education, 3rd edition, 2009.

[3] Q. Fu. Solar radiation. *Academic Press*, pages 1859–1863, 2002.

[4] P. E. Hockberger. A history of ultraviolet photobiology for humans, animals and microorganisms. *Photochem. Photobiol.*, 76(6):561–579, 2002.

[5] M. F. Holick. Vitamin D: importance in the prevention of cancers, type 1 diabetes, heart disease, and osteoporosis. *Am J Clin Nutr.*, 79(3):362–371, 2004.

[6] *Ultraviolet Radiation Guide.* Navy Environmental Health Center 2510 Walmer Avenue Norfolk, Virginia, 1992.

[7] J. F. Waymouth. *Electric discharge lamps.* M.I.T. Press, 1971.

[8] J. Z. Klose, J. M. Bridges, and W. R. Ott. *NBS measurement services: the radiometric standards in the Vacuum Ultraviolet.* Natl. Bur. Stand. (U.S.), Spec. Publ., 1987.

[9] A. Einstein. Concerning an heuristic point of view toward the emission and transformation of light. *Ann. Phys.*, 17, 1905.

[10] G. Suberlucq. Development and production of photo cathodes for the CLIC test facility. *CERN 1211 Geneva 23 Switzerland*, 1996.

[11] *Photomultiplier tubes, basics and applications.* Hamamatsu Photonics K.K., 3rd edition, 2007.

[12] J. L. Wiza. Microchannel plate detectors. *Nucl. Instrum. Methods*, 162:587–601, 1979.

[13] N. Damany, J. Romand, and B. Vodar. *Some Aspects of Vacuum Ultraviolet Radiation Physics.* pergamon Press, 1974.

[14] D. Fishman. *An introduction to circular dichroism spectroscopy.* University of California, Irvine.

[15] *Deep UV Photoresists.* IBM Almaden Research Center, 2006.

[16] R. W. Waynant and M. N. Ediger. *Electro-optics Handbook.* McGraw-Hill, inc., 2nd edition, 2000.

[17] E-E. Koch. *Handbook on Synchrotron Radiation.* North-Holland Amsterdam, 1983.

[18] G. Drake. *Springer handbook of atomic, molecular and optical physics.* Springer Science+Business Media, Inc, 2006.

[19] J. Wilkinson. *New Eyes on the Sun: A Guide to Satellite Images and Amateur Observation.* Astronomers' Universe Series, Springer, 2012.

[20] The Pioneer spacecraft. *NASAFacts. NF-31*, 4(3), 1967.

[21] Pioneer 6, 7, 8, 9, E Quicklook. *Jet Propulsion Laboratory.*

[22] A. R. Morse. MSFC Skylab Apollo Telescope Mount. *NASA technical memorandum*, 1974.

[23] G. M. Sampex et al. SAMPEX: NASA's first small explorer satellite. *IEEE Aerospace Conference*, pages 389–412, 1998.

[24] G. J. Hurford, R. A. Schwartz, S. Krucker, R. P. Lin, D. M. Smith, and N. Vilmer. First gamma-ray images of a solar flare. *The Astrophysical Journal Letters*, 595(2):L77, 2003.

[25] S. Clark. Solar observatory launched to space by japanese rocket. *Spaceflight Now*, 2006.

[26] J. A. Eddy. A new Sun: The Solar Results from Skylab. *Space Flight Center National Aeronautics and Space Administration, Washington, D.C.*, 1979.

[27] R. M. Bonnet and M. Decaudin. High-resolution lyman-alpha filtergrams of the Sun. *Atrophys. J.*, 237:L47–L50, 1980.

[28] R. B. Hoover, Jr. A. B. C. Walker, and Jr T. W. Barbee. Solar Observations with the Multi-Spectral Solar Telescope Array. *SPIE Multilayer and Grazing Incidence X-Ray/EUV Optics*, 1546:175–187, 1991.

[29] K. Wilhelm, W. Curdt, and E. Marsch et al. SUMER - Solar Ultraviolet Measurements of Emitted Radiation. *Sol. Phys.*, 162(1-2):189–231, 1995.

[30] J. L. Kohl, R. Esser, and L. D. gardner. The UtraViolet Coronagraph Spectrometer for the solar and heliospheric observatory. 1996.

[31] E. Quémerais, J.L. Bertaux, and R. Lallement et al. Interplanetary Lyman line profiles derived from SWAN/SOHO hydrogen cell measurements: Full-sky Velocity Field. *J. Geophys. Res.*, 104(A6):12585–12603, 1999.

[32] B. N. Handy, M. E. Bruner, and T. D. Tarbell et al. UV observations with the Transition Region And Coronal Explorer. *Sol. Phys.*, 183:29–43, 1998.

[33] C. M. Korendyke, A. Vourlidas, and J. W. Cook et al. High resolution imaging of the upper solar chromosphere: first ight performance of the Very-high-resolution Advanced Ultraviolet Telescope. *Sol. Phys.*, 200:63–73, 2001.

[34] T. N. Woods and F. G. Eparvier. Solar ultraviolet variability during the TIMED mission Advances in Space Research. *Thermospheric-Ionospheric-Geospheric(TIGER)Symposium*, 37(2):219–224, 2006.

[35] L. J. Paxton, A. B. Christensen, and D. C. Humm et al. Global Ultraviolet Imager (GUVI): Measuring composition and energy inputs for the NASA Thermosphere Ionosphere Mesosphere Energetics and Dynamics (TIMED) mission. *SPIE Opt. Spectrosc. Tech. Instrum. Atmos. Space Res., III*, 3756:265–276, 1999.

[36] M. Snow, W. E. McClintock, and T. N. Woods. Solar spectral irradiance variability in the ultraviolet from SORCE and UARS SOLSTICE. *Adv. Space Res.*, 46(3):296–302, 2010.

[37] *Solar Orbiter Definition study report (Red Book).* Report ESA/SRE, 2011.

[38] D. R. Williams. *Sun Fact Sheet.* NASA Goddard Space Flight Center, 2013.

[39] J. B. Zirker. *Journey from the Center of the Sun.* Princeton University Press, 2002.

[40] M. Romoli, F. Landini, and E. Antonucci et al. METIS: the visible and UV coronagraph for Solar Orbiter. *Proc. of International Conference on Space Optics*, 2014.

[41] G. Hass, W. R. Hunter, and R. Tousey. Reflectance of Evaporated Aluminum in the Vacuum Ultraviolet. *J. Opt. Soc. Am.*, 46(12):1009–1012, 1956.

[42] G. Hass. Reflectance and preparation of front-surface mirrors for use at various angles of incidence from the ultraviolet to the far infrared. *J. Opt. Soc. Am.*, 72(1):27–39, 1982.

[43] G. Hass, W. R. Hunter, and R. Tousey. Influence of Purity, Substrate Temperature, and Aging Conditions on the Extreme Ultraviolet Reflectance of Evaporated Aluminum. *J. Opt. Soc. Am.*, 47(12):1070–1073, 1956.

[44] P. H. Berning, G. Hass, and R. P. Madden. Reflectance-Increasing Coatings for the Vacuum Ultraviolet and Their Applications. *J. Opt. Soc. Am.*, 50(6):586–597, 1960.

[45] E. T. Hutcheson, G. Hass, , and J. T. Cox. Effect of Deposition Rate and Substrate Temperature on the Vacuum Ultraviolet Reflectance of MgF_2- and LiF-Overcoated Aluminum Mirrors. *Appl. Optics*, 11(10):2245–2248, 1972.

[46] S. Ogura, N. Sugawara, and R. Hiraga. Refractive Index and Packing Density for MgF_2 Films: Correlation of Temperature Dependence with Water Sorption. *Thin Solid Films*, 30(3), 1975.

[47] L. R. Canfield, G. Hass, and J. E. Waylonis. Further Studies on MgF_2-Overcoated Aluminum Mirrors with Highest Reflectance in the Vacuum Ultraviolet. *Appl. Optics*, 5(1):45–49, 1966.

[48] M. Fernández-Perea, J. I. Larruquert, and J. A. Aznárez. Vacuum ultraviolet coatings of Al protected with MgF_2 prepared both by ion-beam sputtering and by evaporation. *Appl. Optics*, 40(22):4871–4878, 2007.

[49] A. P. Bradford, G. Hass, and J. F. Osantowski et al. Preparation of Mirror Coatings for the Vacuum Ultraviolet in a 2-m Evaporator. *Appl. Optics*, 8(6):1183–1189, 1969.

[50] P. J. Martin, W. G. Sainty, and R. P. Netterfield et al. Influence of ion assistance on the optical properties of MgF_2. *Appl. Optics*, 26(7):1235–1239, 1987.

[51] E. Antonucci et al. *METIS technical specification.* METIS-OATO-SPE-001, 2013.

[52] M. Fernández-Perea, M. Vidal-Dasilva, and J. I. Larruquert et al. Narrowband filters and broadband mirrors for the spectral range from 50 to 200 nm. *Proc. of SPIE*, 7018(2), 2008.

[53] S. Nannarone, F. Borgatti, and A. DeLuisa et al. The BEAR Beamline at Elettra. *AIP Conference Proceedings*, 705:450–453, 2004.

[54] N. Kaiser. Review of the fundamentals of thin-film growth. *Appl. optics*, 41(16):3053–3060, 2002.

[55] P. B. Barna and M. Adamik. Fundamental structure forming phenomena of polycrystalline films and the structure zone models. *Thin Solid Films*, 317:27–33, 1998.

[56] D. Ristau, S. G'u nster, and S. Bosch et al. Ultraviolet optical and microstructural properties of MgF_2 and LaF_3 coatings deposited by ion-beam sputtering and boat and electron-beam evaporation. *Appl. optics*, 41(16):3196–3204, 2002.

[57] E. D. Palik. *Handbook of Optical Constants of Solids*. Academic press, 1985.

[58] H. J. Hagemann, W. Gudat, and C. Kunz. Optical constants from the Far Infrared to the X-Ray Region: Mg, Al, Cu, Ag, Au, Bi, C, and Al_2O_3. *DESY report SR-74-/7*, 1974.

[59] W. R. Hunter. Optical constants of metals in the Extreme Ultraviolet. II. Optical constants of aluminium, magnesium, and indium at wavelengths shorter than their critical wavelengths. *J. Opt. Soc. Am.*, 54(2):208–212, 1964.

[60] J. I. larruquert, J. A. Méndez, and J. A. Aznárez. Optical constants of aluminium films in the extreme ultraviolet interval of 82-77 nm. *Appl. Optics*, 35(28):5692–5697, 1996.

[61] F. Bridou, M. Cuniot-Ponsard, and J.-M desvignes et al. Experimental determination of optical constants of MgF_2 and AlF_3 thin films in the vacuum ultra-violet wavelength region (60-124 nm), and its application to optical design. *Opt. Commun*, 283:1351–1358, 2010.

[62] O. R. Wood, H. G. Craighead, and J. E. Sweeney. Vacuum ultraviolet loss in magnesium fluoride films. *Appl. Optics*, 23(20):3644–3649, 1984.

[63] D. Fabre, J. Romand, and B. Vodar. Mesures des constantes optiques de dépote évaporés de fluorure de magnesium dans l'ultraviolet de Schumann. *Opt. Acta*, 9(73), 1962.

[64] D. L. Windt. IMD-Software for modeling the optical properties of multilayer films. *Comput. Phys.*, 12(4):360–370, 1998.

[65] P. D. Binda and F. E. Zocchi. Genetic algorithm optimization of X-ray multilayer coatings. *Proceedings of SPIE*, 5536:97–108, 2004.

[66] J. F. O'Hanlon. *A User's Guide to Vacuum Technology*. John Wiley and Sons, 3rd edition, 2005.

[67] M. R. Adriaens and B. Feuerbacher. Improved LiF and MgF2 Overcoated Aluminum Mirrors for Vacuum Ultraviolet Astronomy. *Appl. Optics*, 10(4):958–959, 1971.